Visual Orbits of Spectroscopic Binaries with the CHARA Array. IV. HD 61859, HD 89822, HD 109510, and HD 191692

Kathryn V. Lester, Gail H. Schaefer, Francis C. Fekel, Douglas R. Gies, Todd J. Henry, Wei-Chun Jao, Leonardo A. Paredes, Hodari-Sadiki Hubbard-James, Christopher D. Farrington, Kathryn D. Gordon, et al.

The Astronomical Journal, 164:228 (20pp), 2022 December https://doi.org/10.3847/1538-3881/ac9385

Visual Orbits of Spectroscopic Binaries with the CHARA Array. IV. HD 61859, HD 89822, HD 109510, and HD 191692

Kathryn V. Lester[1], Gail H. Schaefer[2], Francis C. Fekel[3], Douglas R. Gies[4], Todd J. Henry[5], Wei-Chun Jao[6], Leonardo A. Paredes[6], Hodari-Sadiki Hubbard-James[6], Christopher D. Farrington[2], Kathryn D. Gordon[7], S. Drew Chojnowski[8], John D. Monnier[9], Stefan Kraus[10], Jean-Baptiste Le Bouquin[11], Narsireddy Anugu[2], Theo Ten Brummelaar[2], Claire L. Davies[10], Tyler Gardner[9], Aaron Labdon[12], Cyprien Lanthermann[2], and Benjamin R. Setterholm[9]

[1] NASA Ames Research Center, Moffett Field, CA 94035, USA; kathryn.v.lester@nasa.gov
[2] The CHARA Array of Georgia State University, Mount Wilson Observatory, Mount Wilson, CA 91023, USA
[3] Center of Excellence in Information Systems, Tennessee State University, Nashville, TN 37209, USA
[4] Center for High Angular Resolution Astronomy and Department of Physics & Astronomy, Georgia State University, Atlanta, GA 30302, USA
[5] RECONS Institute, Chambersburg, PA 17201, USA
[6] Department of Physics & Astronomy, Georgia State University, Atlanta, GA 30302, USA
[7] University of Tampa, Tampa, FL 33606, USA
[8] Department of Physics, Montana State University, Bozeman, MT 59717, USA
[9] Department of Astronomy, University of Michigan, Ann Arbor, MI 48109, USA
[10] Astrophysics Group, Department of Physics & Astronomy, University of Exeter, Exeter, EX4 4QL, UK
[11] Univ. Grenoble Alpes, CNRS, IPAG, 38000, Grenoble, France
[12] European Southern Observatory, Casilla 19001, Santiago 19, Chile
Received 2022 September 7; revised 2022 September 19; accepted 2022 September 19; published 2022 November 1

Abstract

We present the visual orbits of four spectroscopic binary stars, HD 61859, HD 89822, HD 109510, and HD 191692, using long baseline interferometry with the CHARA Array. We also obtained new radial velocities from echelle spectra using the APO 3.5 m, CTIO 1.5 m, and Fairborn Observatory 2.0 m telescopes. By combining the astrometric and spectroscopic observations, we solve for the full, three-dimensional orbits and determine the stellar masses to 1%–12% uncertainty and distances to 0.4%–6% uncertainty. We then estimate the effective temperature and radius of each component star through Doppler tomography and spectral energy distribution analyses. We found masses of 1.4–3.5 $M_{\odot}$, radii of 1.5–4.7 $R_{\odot}$, and temperatures of 6400–10,300 K. We then compare the observed stellar parameters to the predictions of the stellar evolution models, but found that only one of our systems fits well with the evolutionary models.

Unified Astronomy Thesaurus concepts: Binary stars (154); Spectroscopic binary stars (1557); Visual binary stars (1777); Long baseline interferometry (932); Fundamental parameters of stars (555)

1. Introduction

We continue our paper series of determining the visual orbits of spectroscopic binary stars with long baseline interferometry —Paper I (Lester et al. 2019a), Paper II (Lester et al. 2019b), and Paper III (Lester et al. 2020)—in order to determine the fundamental stellar parameters of the components. Precise fundamental parameters of binary systems are essential for determining orbital demographics (Raghavan et al. 2010; Bordier et al. 2022), testing models of stellar structure and evolution (e.g., Claret & Torres 2018; Morales et al. 2022), calibrating mass and distance determination methods for single stars (Torres et al. 2010; Chaplin & Miglio 2013; Gallenne et al. 2018), and studying how binary stars form and evolve (e.g., Richardson et al. 2021). In this paper, we present the results for the more massive binaries, HD 61859, HD 89822, HD 109510, and HD 191692. Higher-mass stars evolve rather quickly, so matching the observed parameters of both components at the same age becomes more challenging for evolutionary models.

HD 61859 (HR 2962, HIP 37580) consists of a pair of F-type stars in a 32 day orbit. The first spectroscopic orbit was measured by Harper (1926), then more recently updated by Tomkin & Fekel (2008) using high-resolution echelle spectra.

HD 89822 (ET UMa, HR 4072, HIP 50933) is a well-studied binary consisting of an early A-type star and an early F-type star in a 12 day orbit. Spectroscopic orbits were determined by Schlesinger (1912) and Nariai (1970). The primary component of HD 89822 was identified as a Mercury-Manganese (HgMn) star (Abt & Snowden 1973), the higher-mass cousins of metallic line (Am) stars. Adelman (1994) completed a detailed abundance analysis of the system to confirm this classification and found that the secondary is an Am star (see also Chojnowski et al. 2020). The TESS light curve of HD 89822 also shows a heartbeat pattern (Kochukhov et al. 2021; Kołaczek-Szymański et al. 2021), which is a brightening near periastron due to tidal distortion in close eccentric binaries (Thompson et al. 2012), but the system shows no evidence of the rotational modulation found in some HgMn stars (Kochukhov et al. 2021).

HD 109510 (24 Com B, HR 4791, HIP 61415) contains a pair of A-type stars in a 7 day orbit. HD 109510 has been studied spectroscopically by Petrie (1937) and Mayor & Mazeh (1987). HD 109510 also has a bright visual companion, HD 109511 (24 Com A), at a separation of 20″. This star has

a similar proper motion, radial velocity, and parallax to HD 109510, so they are likely physically associated. However, HD 109511 is beyond the fields of view of our telescopes and will not affect our observations. The timescales of the inner orbits are also much shorter than that of the outer pair, so HD 109511 would not cause visible perturbations in the orbit of HD 109510.

HD 191692 (θ Aql, HR 7710, HIP 99473) contains a pair of late B-type stars in a 17 day orbit. A spectroscopic orbit was measured by Cesco & Struve (1946) and a visual orbit was measured by Hummel et al. (1995) using the Mark III interferometer; Pourbaix (2000) later used these observations to determine a combined (VB+SB2) orbital fit. However, these observations lack the high spectral and angular resolution of modern day echelle spectrographs and long baseline interferometers, so new observations will provide more precise results. In addition, a detailed abundance analysis of HD 191692 was completed by Adelman et al. (2015), which found the primary component to have solar abundances and the secondary component to be weakly metallic lined.

In Section 2, we present our spectroscopic observations and radial velocities. In Section 3, we describe our interferometric observations, binary position measurements, and combined orbital solution. In Section 4, we determine the fundamental stellar parameters of each component and compare the results to stellar evolution models. Finally, we discuss our results in Section 5.

2. Spectroscopy

2.1. APO Observations

We observed HD 61859, 89822, and 109510 with the ARC echelle spectrograph (ARCES; Wang et al. 2003) on the APO 3.5 m telescope from 2015 to 2020. ARCES covers 3500–10,500 Å over 107 orders at an average resolving power of $R \sim 30,000$. We reduced our data using standard echelle procedures in IRAF, then removed the blaze function using the procedure in Appendix A of Kolbas et al. (2015). Radial velocities (V_{r1}, V_{r2}) were measured with the multi-order TODCOR method (Zucker & Mazeh 1994; Zucker et al. 2003) as described in Paper II. In summary, TODCOR calculates the cross-correlation function (CCF) for a grid of primary and secondary radial velocities. The CCFs for each echelle order were added together to find the maximum CCF, corresponding to the best-fit radial velocities and their uncertainties (σ_1, σ_2). Templates were created with the use of BLUERED model spectra (Bertone et al. 2008) and atmospheric parameters from recent literature. Our observations are listed in the Appendix. TODCOR also calculates the monochromatic flux ratio (f_2/f_1) near Hα, which we use later to estimate the radius ratio for each system (see Section 4.3).

2.2. CTIO Observations

We observed HD 109510 and 191692 with the CHIRON echelle spectrograph (Tokovinin et al. 2013; Paredes et al. 2021) on the CTIO/SMARTS 1.5 m telescope from 2014 to 2020. HD 109510 was observed in the $R \sim 28,000$ fiber mode and HD 191692 was observed in the $R \sim 90,000$ slicer mode. Both modes cover 4500–8800 Å over 60 echelle orders. The data were reduced with the CHIRON team's pipeline, then we used the above procedure to remove the blaze function and measure radial velocities of each component. These observations are also listed in the Appendix.

2.3. Fairborn Observations

We also acquired spectroscopic observations of all four binaries at Fairborn Observatory in southeast Arizona with the Tennessee State University 2.0 m Automatic Spectroscopic Telescope (AST) and a fiber-fed echelle spectrograph (Eaton & Williamson 2004). We obtained spectra of HD 61859 from 2011 to 2020 as a continuation of the velocities published by Tomkin & Fekel (2008). We collected spectra of HD 89822 from 2005 to 2020, HD 109510 from 2020 to 2021, and of HD 191692 from 2004 to 2021. The observations of HD 89822 and HD 191692 that were obtained before 2011 were acquired with a 2048×4096 SITe ST-002A CCD. Those spectra have 21 orders, cover a wavelength region of 4920–7100 Å, and have $R \sim 35,000$ at 6000 Å. During the summer of 2011 we replaced the SITe CCD with a Fairchild 486 CCD that has a 4096×4096 pixel array enabling coverage of a wavelength range of 3800–8600 Å over 48 orders (Fekel et al. 2013). We used a 200 μm fiber that produced $R \sim 25,000$ at 6000 Å. Eaton & Williamson (2007) explained the data reduction and wavelength calibration of the raw AST spectra.

Fekel et al. (2009) provided a general description of the typical velocity reduction. Briefly, for HD 61859 and HD 109510 we used a solar-type star line list consisting of 168 mostly neutral Fe lines in the wavelength region 4920–7100 Å. The early-A and late-B spectral classes of the components of HD 89822 and HD 191692 required the use of our A-star line list. The lines in that list cover the same wavelength region as the solar-type line list but mainly include ionized Fe lines. Each line was fitted with a rotational broadening function (Sandberg Lacy & Fekel 2011), and if the lines of the two components were partly blended we obtained a simultaneous fit. The stellar velocity was determined as the average of the line fits. A value of 0.3 km s^{-1} was added to the SITe CCD velocities and 0.6 km s^{-1} to the Fairchild CCD velocities to make the resulting velocities from the two CCDs consistent with the velocity zero-point of Scarfe (2010). These observations are also listed in the Appendix.

2.4. Preliminary Spectroscopic Orbit

Following the procedure in previous papers, we accounted for differences in the zero-point offset of each spectrograph by first fitting separate orbital solutions to each data set using the RVFIT program[13] (Iglesias-Marzoa et al. 2015). We solved for the six spectroscopic orbital parameters of each system: the orbital period (P), epoch of periastron (T), eccentricity (e), longitude of periastron of the primary star (ω_1), velocity semiamplitudes (K_1, K_2), and systemic velocity (γ). We also fit an orbit to the previously published velocities of HD 61859 from Tomkin & Fekel (2008) using preliminary uncertainties equal to $1/\sqrt{\text{weight}}$. We shifted the APO, CTIO, and literature data sets such that the systemic velocities match those of the Fairborn data sets. We then used the χ^2 values from the individual solutions to rescale the uncertainties such that the reduced χ^2 of each data set equals one. Our adjusted velocities and rescaled uncertainties are those listed in the Appendix.

[13] http://www.cefca.es/people/~riglesias/rvfit.html

Table 1
Relative Positions

Target	UT Date	HJD-2,400,000	ρ (mas)	θ (deg)	σ_{maj} (mas)	σ_{min} (mas)	ϕ (deg)	f_2/f_1	Beam Combiner
HD 61859	2013 Dec 11	56638.0297	2.531	63.3	0.253	0.056	83.6	0.410 ± 0.003	CLIMB
HD 61859	2017 Feb 01	57785.7409	3.719	242.1	0.169	0.101	51.7	0.406 ± 0.009	CLIMB
HD 61859	2017 Nov 30	58087.8801	2.961	60.5	0.171	0.092	130.9	0.390 ± 0.005	CLIMB
HD 61859	2018 Dec 12	58464.8835	2.494	63.4	0.171	0.083	56.2	0.431 ± 0.014	CLIMB
HD 61859	2019 Sep 18	58745.0249	0.430	140.0	0.226	0.226	144.5	0.574 ± 0.180	CLIMB
HD 61859	2019 Dec 21	58838.8581	0.696	194.7	0.270	0.115	57.8	...	CLIMB
HD 61859	2021 Mar 28	59301.6728	5.027	237.4	0.001	0.001	153.4	0.3852 ± 0.0002	MIRC-X
HD 89822	2017 Nov 30	58088.0567	1.884	282.1	0.131	0.104	28.3	0.214 ± 0.008	CLIMB
HD 89822	2018 Apr 10	58218.7122	1.002	166.8	0.110	0.027	164.4	0.232 ± 0.002	CLIMB
HD 89822	2018 Apr 11	58219.7138	1.128	122.2	0.115	0.058	100.1	0.231 ± 0.004	CLIMB
HD 89822	2018 Nov 26	58449.0307	1.206	227.7	0.063	0.049	153.5	0.263 ± 0.005	CLIMB
HD 89822	2018 Dec 12	58464.9750	1.315	22.7	0.069	0.059	150.6	0.267 ± 0.005	CLIMB
HD 89822	2019 Apr 25	58598.7623	1.386	259.3	0.067	0.034	110.4	0.339 ± 0.011	CLIMB
HD 89822	2019 Apr 26	58599.6880	1.207	224.8	0.082	0.050	43.0	0.396 ± 0.030	CLIMB
HD 89822	2019 Apr 27	58600.7010	1.060	170.9	0.114	0.058	138.3	0.245 ± 0.004	CLIMB
HD 89822	2019 Apr 28	58601.7970	1.087	115.6	0.219	0.087	115.5	0.278 ± 0.007	CLIMB
HD 89822	2019 Dec 20	58838.0461	2.071	322.4	0.087	0.052	72.0	0.208 ± 0.003	CLIMB
HD 89822	2021 Mar 28	59301.7480	2.106	319.5	0.001	0.001	143.1	0.2276 ± 0.0001	MIRC-X
HD 109510	2017 May 20	57893.7031	0.680	167.6	0.267	0.090	161.4	0.471 ± 0.102	CLIMB
HD 109510	2017 May 21	57894.7054	0.587	285.4	0.134	0.066	111.5	0.458 ± 0.065	CLIMB
HD 109510	2019 Apr 26	58599.8104	0.831	319.7	0.027	0.014	136.6	0.561 ± 0.011	CLIMB
HD 109510	2019 Apr 27	58600.8133	0.689	354.2	0.041	0.021	102.5	0.579 ± 0.015	CLIMB
HD 109510	2021 Mar 28	59301.8264	0.935	146.8	0.001	0.001	168.7	0.5285 ± 0.0002	MIRC-X
HD 191692	2012 Sep 04	56174.6984	1.375	296.1	0.383	0.240	130.9	0.181 ± 0.012	CLIMB
HD 191692	2017 Sep 08	58004.6859	2.795	17.7	0.236	0.236	121.0	0.235 ± 0.001	CLIMB
HD 191692	2018 Aug 17	58347.8136	2.308	4.8	0.248	0.136	15.9	0.260 ± 0.003	CLIMB
HD 191692	2018 Sep 03	58364.6972	2.439	9.8	0.201	0.178	112.6	0.245 ± 0.004	CLIMB
HD 191692	2018 Sep 05	58366.6994	1.337	287.9	0.293	0.188	141.2	0.169 ± 0.002	CLIMB
HD 191692	2019 Jul 04	58668.9676	4.383	55.8	0.007	0.002	50.2	0.238 ± 0.001	MIRC-X
HD 191692	2019 Sep 16	58742.6754	1.701	330.8	0.496	0.252	41.1	0.177 ± 0.004	CLIMB
HD 191692	2020 Aug 12	59073.7005	4.111	95.3	0.006	0.002	141.9	0.2415 ± 0.0001	MIRC-X
HD 191692	2020 Aug 13	59074.6859	4.476	88.2	0.010	0.004	147.9	0.2235 ± 0.0003	MIRC-X

3. Interferometry

3.1. CHARA Array Observations

We observed all four binaries with the CHARA Array from 2012 to 2019 using the CLIMB (ten Brummelaar et al. 2013) beam combiner and from 2019 to 2021 using the MIRC-X (Anugu et al. 2020) beam combiner. CHARA has six 1.0 m telescopes arranged in a Y-shape with baselines ranging from 34 to 331 m (ten Brummelaar et al. 2005). CLIMB combines the K'-band light from three telescopes at a time, while MIRC-X combines the H-band light from up to six telescopes and disperses the light into six narrowband spectral channels at $R = 50$. Table 1 lists the UT date, HJD, and beam combiner for each CHARA observation. The CLIMB data were reduced with the pipeline developed by John D. Monnier; the general method is described in Monnier et al. (2011) and the extension to three beams is described in Kluska et al. (2018). The MIRC-X data were reduced using the pipeline (version 1.3.3–1.3.5) developed by Jean-Baptiste Le Bouquin and the MIRC-X team,[14] which splits each 10 minutes data sequence into four 2.5 minutes bins. These reductions produce squared visibilities (V^2) for each baseline and closure phases (CP) for each closed triangle. We corrected for any instrumental and atmospheric effects on the observed visibilities using observations of calibrators stars, whose uniform-disk angular diameters were taken from SearchCal (Chelli et al. 2016), and are listed in the Appendix. On each night, we also calibrated the calibrators against each other and did not find evidence of binarity in the calibrators.

3.2. Binary Positions

We measured the relative positions from the visibilities and closure phases using the method[15] of Schaefer et al. (2016), which searches across a grid of separations in R.A. and decl. to find the best-fit relative position. At each grid point, we compared the observed V^2 and CP to model values to fit for the flux ratio and calculate the χ^2 value. We then searched a small area around the best-fit position to find the contour marking $\chi^2 \leqslant \chi^2_{min} + 1$ that determines the major axis (σ_{maj}), minor axis (σ_{min}), and position angle (ϕ) of each error ellipse. Because the orbital periods of these systems are much longer than the observation time, any small orbital motion within a single night is contained within the error ellipses. The best-fit relative positions, error ellipse parameters, and flux ratio estimates for each night are listed in Table 1.

[14] https://gitlab.chara.gsu.edu/lebouquj/mircx_pipeline.git

[15] http://www.chara.gsu.edu/analysis-software/binary-grid-search

Table 2
Orbital Parameters from VB+SB2 Solution

Parameter	HD 61859	HD 89822	HD 109510	HD 191692
P (days)	31.500002 ± 0.000056	11.579113 ± 0.000010	7.336673 ± 0.000087	17.124281 ± 0.000038
T (HJD-2400000)	58880.701 ± 0.018	57756.168 ± 0.005	59361.967 ± 0.011	58624.154 ± 0.004
e	0.1951 ± 0.0007	0.2943 ± 0.0009	0.2585 ± 0.0012	0.6040 ± 0.0009
ω_1 (deg)	39.52 ± 0.23	176.50 ± 0.20	302.33 ± 0.28	33.73 ± 0.22
i (deg)	94.73 ± 3.51	141.87 ± 0.97	61.40 ± 3.89	144.10 ± 0.18
α (mas)	4.403 ± 0.003	1.634 ± 0.001	1.007 ± 0.037	3.148 ± 0.002
Ω (deg)	237.81 ± 3.45	133.49 ± 0.13	136.17 ± 2.86	96.92 ± 0.19
γ (km s^{-1})	−12.51 ± 0.03	−2.24 ± 0.03	3.51 ± 0.06	−29.26 ± 0.08
K_1 (km s^{-1})	46.77 ± 0.07	38.17 ± 0.04	68.16 ± 0.09	48.78 ± 0.09
K_2 (km s^{-1})	52.81 ± 0.03	62.11 ± 0.09	81.28 ± 0.20	63.48 ± 0.11

We note that the flux ratios are likely underestimated, because they do not account for systematics in visibility miscalibrations. Furthermore, the more precise CP of MIRC-X can constrain the flux ratios better than CLIMB, so we used the flux ratios from the MIRC-X observations to estimate the radius ratios in Section 4.3. We calculated the uncertainty for a single measurement from the standard deviation of the flux ratios derived from the three MIRC-X observations of HD 191692. We used this value as the final uncertainty for HD 61859, HD 89822, and HD 109510, but scaled this value by $\sqrt{3}$ to calculate the final uncertainty for HD 191692.

For HD 191692, the primary star is large enough to be resolved by CHARA, so we simultaneously fit the V^2 and CP for the primary angular diameter (θ_1) and the binary parameters. The secondary component is unresolved, so we held the angular diameter fixed to $\theta_2 = 0$ mas. We found the weighted-mean, uniform-disk angular diameter to be $\theta_1 = 0.571 \pm 0.017$ mas from our MIRC-X observations. We also tested limb-darkened models using linear limb-darkening coefficients from Claret (2000) for the effective temperature and surface gravity found in Section 4.3. However, the difference between the limb-darkened visibilities and the uniform-disk visibilities were roughly ten times smaller than the observational uncertainties, because limb darkening is very weak in the near-infrared (Davis et al. 2000).

3.3. Combined Visual + Spectroscopic Solution

We determined the final orbital solution by simultaneously fitting the interferometric and spectroscopic data using the method[16] of Schaefer et al. (2016). The full set of orbital parameters includes the orbital period (P), epoch of periastron (T), eccentricity (e), longitude of periastron of the primary star (ω_1), the inclination (i), the angular semimajor axis (a), the longitude of the ascending node (Ω), the systemic velocity (γ), and the velocity semiamplitudes (K_1, K_2). Table 2 lists the combined (VB+SB2) orbital solutions for each system. The visual orbits of all four systems are shown in Figure 1 and the spectroscopic orbits are shown in Figure 2. To determine the uncertainty of each orbital parameter, we performed a Monte Carlo error analysis in which we varied each data point within its Gaussian uncertainty and refit for the orbital solution. We then made a histogram of the best-fit parameters from 10^5 iterations and fit Gaussians to each distribution to determine the 1σ uncertainties in each parameter (also listed in Table 2).

[16] https://www.chara.gsu.edu/analysis-software/orbfit-lib

4. Stellar Parameters

4.1. Masses and Distance

We calculated the component masses and binary distance from the combined orbital solution using nominal Solar values from Prša et al. (2016). Our results are listed in Table 3. The uncertainties in component mass are less than 1.4% for HD 61859, 5.5% for HD 89822, 11.9% for HD 109510, and 1.4% for HD 191692. The uncertainties in distance are 0.5% for HD 61859, 2.0% for HD 89822, 5.6% for HD 109510, and 0.4% for HD 191692.

Model independent distance measurements from binary stars are important checks for other distances measurements, such as the Cepheid period–luminosity relationship (Gallenne et al. 2018) and trigonometric parallax (Halbwachs et al. 2016; Stassun & Torres 2018). We compared our distances from orbital parallax to the distances from Gaia DR3 parallaxes (Gaia Collaboration et al. 2016, 2022), which are listed at the end of Table 3. Our distances were consistent with Gaia's to within the 1σ uncertainties for HD 61859, HD 89822, and HD 109510. However, our distance for HD 191692 of 76.3 ± 0.3 pc does not match the Gaia distance of 70.1 ± 2.3 pc. HD 191692 is a very bright star ($G = 3.2$ mag), so the trigonometric parallax could have been affected by saturation.

4.2. Atmospheric Parameters

We reconstructed the spectra of each binary component using the method of Bagnuolo et al. (1992) as described in Papers I–III. Initial model templates were created using atmospheric parameters from the recent literature. We then fit for the effective temperature ($T_{\rm eff}$), projected rotational velocity ($V \sin i$), and metal abundance ($\log Z/Z_\odot$) of each component by cross-correlating a grid of BLUERED model spectra against the reconstructed spectra. Only echelle orders in the range 4500–6600 Å that contain strong absorption lines were used. We determined the best-fit parameters of each component and their uncertainties from the CCF peak, as listed in Table 3. Example plots of the final reconstructed spectra and best-fit model spectra are shown in the Appendix. For HD 61859, we found both components to be slightly metal-poor. We found HD 89822 to have a slightly metal-rich primary and a roughly Solar abundance secondary, consistent with the iron abundances found by Adelman (1994). We also confirm that the primary component is a HgMn star and the secondary component is an Am star based on the reconstructed spectra. Both components of HD 109510 are also slightly metal-poor,

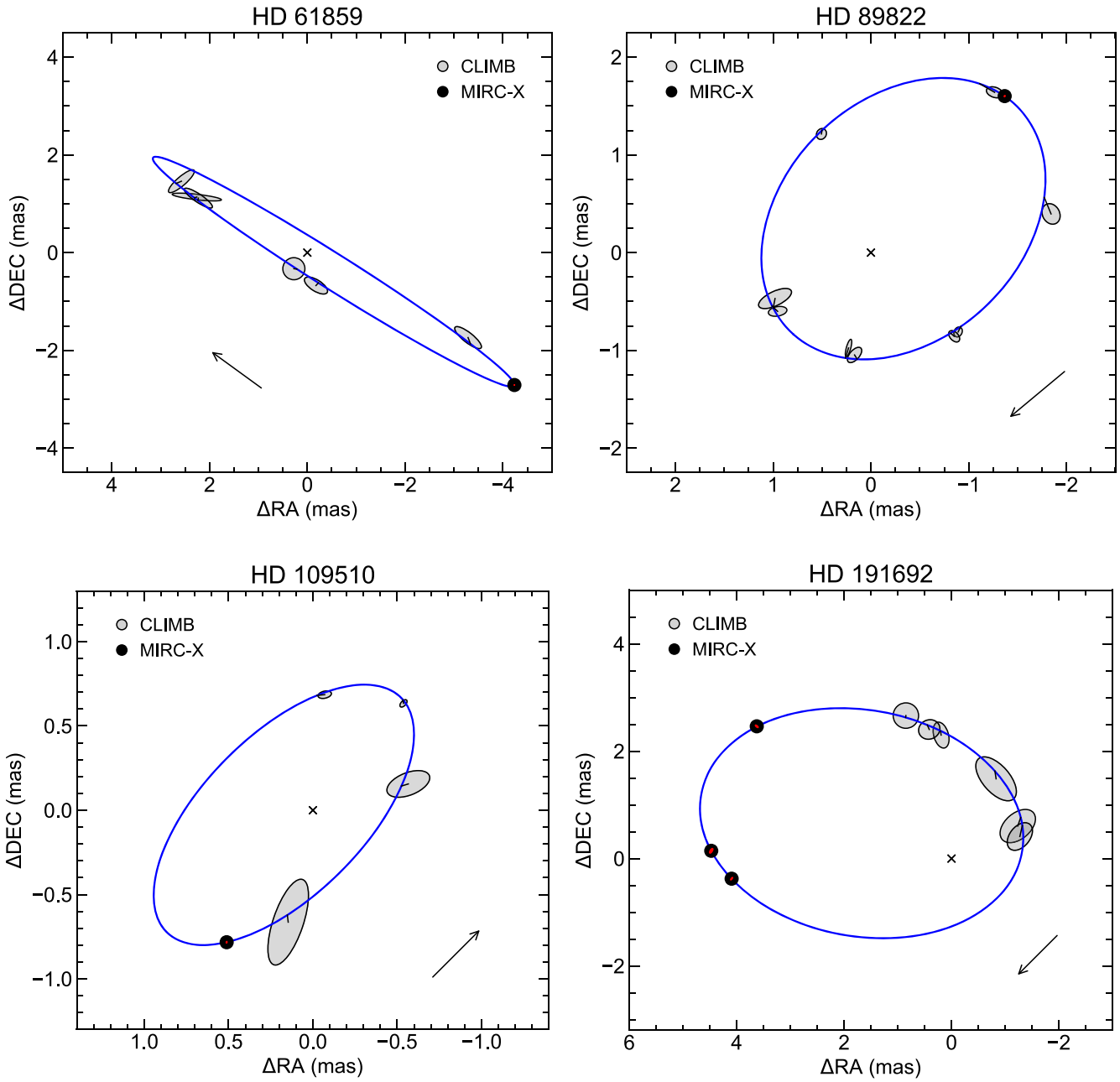

Figure 1. Visual orbits of HD 61859 (top left), HD 89822 (top right), HD 109510 (bottom left), and HD 191692 (bottom right). The primary star is located at the origin (black cross). The relative positions of the secondary star from CLIMB data are marked by the gray points corresponding to the sizes of the error ellipses. The relative positions from MIRC-X data are marked by black circles with red error ellipses, which are often to small to be seen. The solid blue curves represent the best-fit model visual orbits, and thin black lines connect each observed and model position. The arrows indicate the directions of orbital motion.

but the secondary is consistent with Solar metallicity within the uncertainties. Finally, we found both components of HD 191692 to be slightly metal-rich, consistent with the iron abundances found by Adelman et al. (2015).

4.3. Radii and Surface Gravities

We built spectral energy distributions (SEDs) using photometry from the literature in order to determine the radii of each component. We included UV photometry from the TD1 Stellar Ultraviolet Fluxes Catalog (Thompson et al. 1978), optical photometry from the Fourth US Naval Observatory CCD Astrograph Catalog (Zacharias et al. 2013), and infrared photometry from the Two Micron All Sky Survey (Skrutskie et al. 2006), and the Wide-field Infrared Survey Explorer (Wright et al. 2010). The data set for HD 109510 also includes low resolution, flux calibrated spectroscopy from Burnashev (1985).

Next, we created surface flux models of each component (Castelli & Kurucz 2004) based on the $T_{\rm eff}$ found above. We estimated the radius ratio (R_2/R_1) of each binary by comparing the model surface flux ratio and the observed flux ratios near $H\alpha$ (from spectroscopy) and in the H band (from interferometry). These parameters are listed in Table 4. The surface flux models were also used to create a combined, binary SED model for each system. Using the procedure described in Paper III, we fit the binary model SED to the observed fluxes in order to determine the angular diameter of the primary star (θ_1) and the

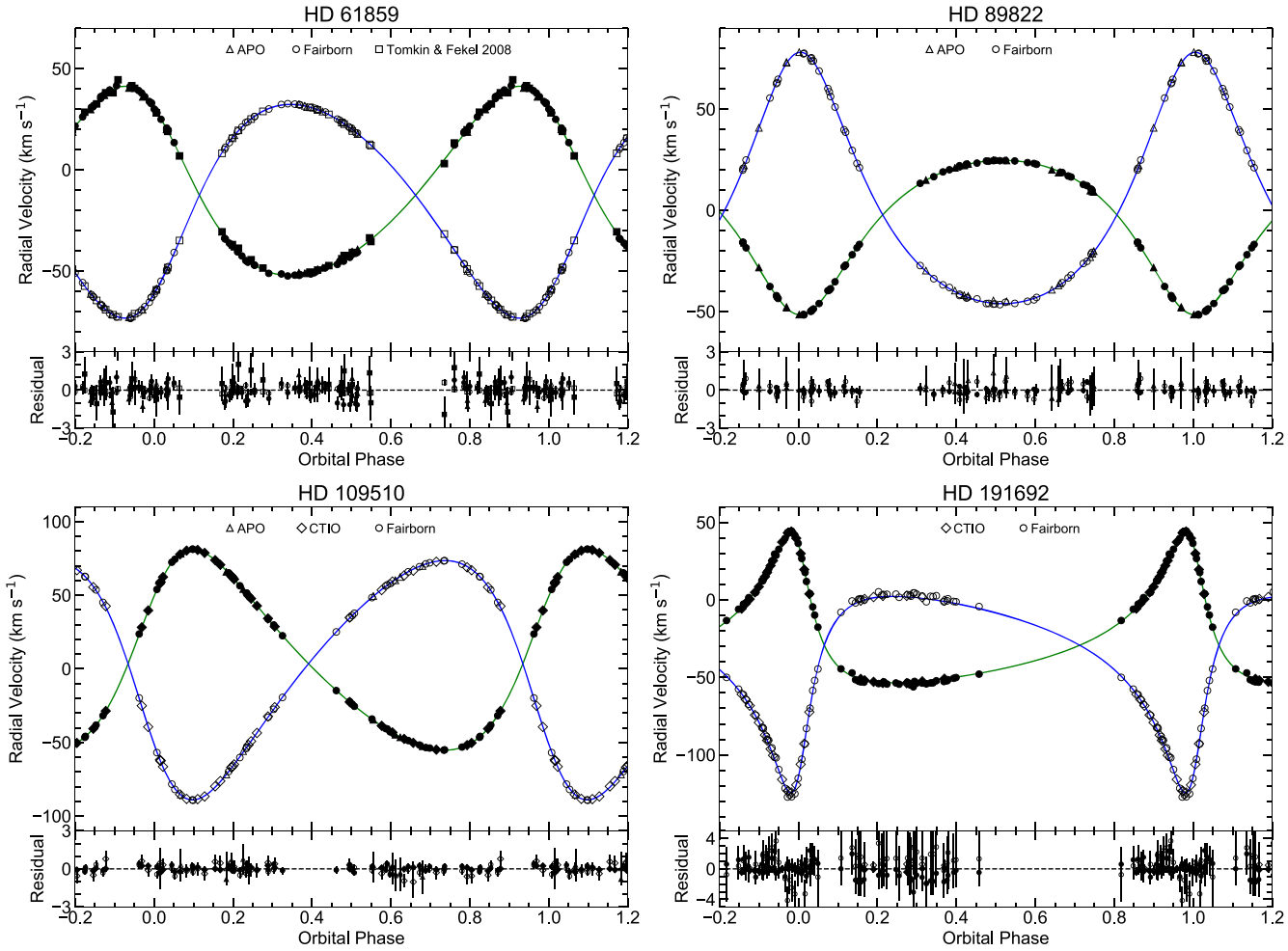

Figure 2. Radial velocity curves of HD 61859 (top left), HD 89822 (top right), HD 109510 (bottom left), and HD 191692 (bottom right). The observed data for the primary and secondary star are shown with the filled and open points, respectively. The triangles, diamonds, and circles represent the APO, CTIO, and Fairborn data, respectively. The model curves are shown with the solid lines, and the residuals to the fit are shown in the bottom panels.

Table 3
Astrophysical Parameters

Parameter	HD 61859	HD 89822	HD 109510	HD 191692
M_1 ($M_\odot$)	1.629 ± 0.023	2.779 ± 0.153	1.838 ± 0.218	3.564 ± 0.049
M_2 ($M_\odot$)	1.443 ± 0.020	1.708 ± 0.094	1.541 ± 0.184	2.739 ± 0.037
R_1 ($R_\odot$)	2.53 ± 0.10	3.16 ± 0.11	2.28 ± 0.06	4.76 ± 0.14
R_2 ($R_\odot$)	1.51 ± 0.06	1.73 ± 0.06	1.70 ± 0.07	2.34 ± 0.07
$T_{\rm eff\ 1}$ (K)	6390 ± 180	10260 ± 100	7630 ± 120	10300 ± 200
$T_{\rm eff\ 2}$ (K)	6610 ± 230	7860 ± 140	7180 ± 140	10230 ± 220
$\log g_1$ (cgs)	3.85 ± 0.02	3.88 ± 0.05	3.86 ± 0.01	3.64 ± 0.02
$\log g_2$ (cgs)	4.22 ± 0.02	4.22 ± 0.05	4.09 ± 0.02	4.14 ± 0.02
L_1 ($L_\odot$)	9.6 ± 1.3	101.0 ± 8.0	15.6 ± 1.3	229.8 ± 22.5
L_2 ($L_\odot$)	4.1 ± 0.5	9.7 ± 1.0	7.2 ± 0.9	54.0 ± 5.8
$V_1 \sin i$ (km s^{-1})	37.1 ± 1.0	$\leqslant 4.2$	14.5 ± 1.5	36.3 ± 0.4
$V_2 \sin i$ (km s^{-1})	$\leqslant 4.2$	5.1 ± 2.1	14.2 ± 1.1	13.6 ± 0.9
$\log Z_1/Z_\odot$ (dex)	-0.05 ± 0.12	0.11 ± 0.04	-0.05 ± 0.02	0.05 ± 0.05
$\log Z_2/Z_\odot$ (dex)	-0.06 ± 0.05	-0.05 ± 0.07	-0.04 ± 0.07	0.12 ± 0.13
Distance (pc, this work)	64.4 ± 0.3	101.1 ± 2.0	110.1 ± 6.1	76.3 ± 0.3
Distance (pc, Gaia DR3)	64.8 ± 1.9	103.8 ± 1.0	111.8 ± 0.4	70.1 ± 2.3

color excess ($E(B-V)$) of each system. For HD 191692, we converted the uniform-disk angular diameter of the primary component measured directly with interferometry to a limb-darkened disk diameter (Davis et al. 2000), then held this parameter fixed to fit only for reddening. We then used the radius ratios to calculate the angular diameters of the secondary stars (θ_2). The observed SED's and best-fit models are shown in Figure 3, and the best-fit SED parameters are listed in Table 4.

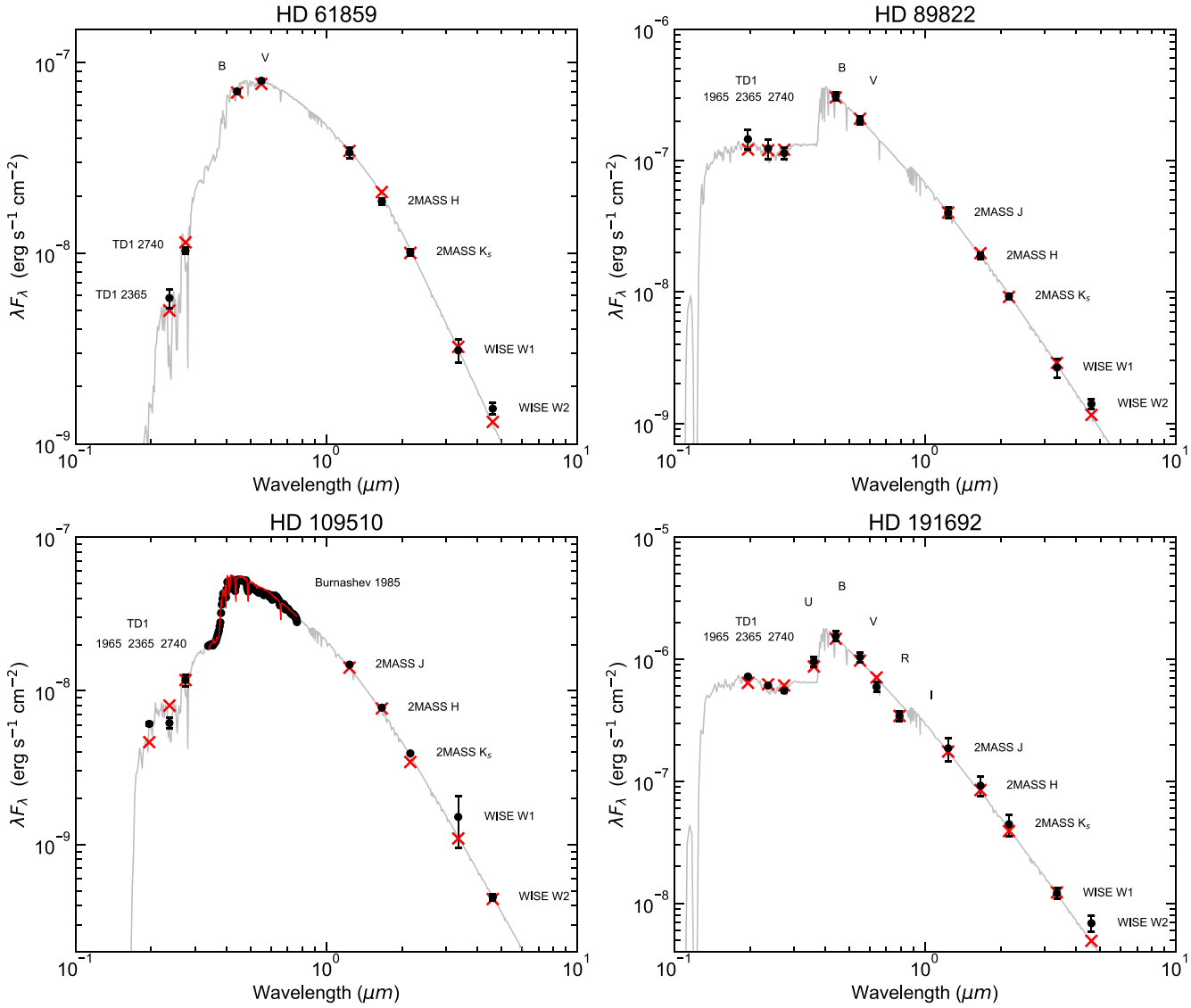

Figure 3. SEDs of HD 61859 (top left), HD 89822 (top right), HD 109510 (bottom left), and HD 191692 (bottom right). The observed fluxes are shown in black, and the best-fit binary model fluxes are shown as the red crosses. The full binary model is shown in gray. For clarity, we do not show the uncertainties in the Burnashev (1985) spectra of HD 109510.

Table 4
SED Parameters

Parameter	HD 61859	HD 89822	HD 109510	HD 191692
f_2/f_1 (6500 Å)	0.45 ± 0.03	0.18 ± 0.07	0.70 ± 0.05	0.25 ± 0.06
f_2/f_1 (H-band)	0.385 ± 0.007	0.228 ± 0.007	0.526 ± 0.007	0.238 ± 0.004
R_2/R_1	0.60 ± 0.01	0.55 ± 0.01	0.75 ± 0.02	0.49 ± 0.01
θ_1 (mas)	0.363 ± 0.014	0.291 ± 0.009	0.189 ± 0.005	0.580 ± 0.017[a]
θ_2 (mas)	0.217 ± 0.009	0.159 ± 0.005	0.142 ± 0.007	0.285 ± 0.009
$E(B-V)$	0.05 ± 0.01	0.01 ± 0.02	0.01 ± 0.01	0.00 ± 0.01

Note.
[a] Fixed to the limb-darkened angular diameter from CHARA observations.

Finally, we combined the Gaia DR3 distances with the angular diameters to calculate the component radii, except in the case of HD 191692. The Gaia parallax of HD 191692 does not agree with our results and has a larger uncertainty, so we used the distance from orbital parallax instead. Table 3 lists the best-fit stellar radii of each component, the surface gravities calculated from the masses and radii, and the luminosities calculated from the Stefan–Boltzmann law. Our stellar radii have uncertainties less than 4.0% for HD 61859, 3.6% for HD 89822, 4.1% for HD 109510, and 3.0% for HD 191692.

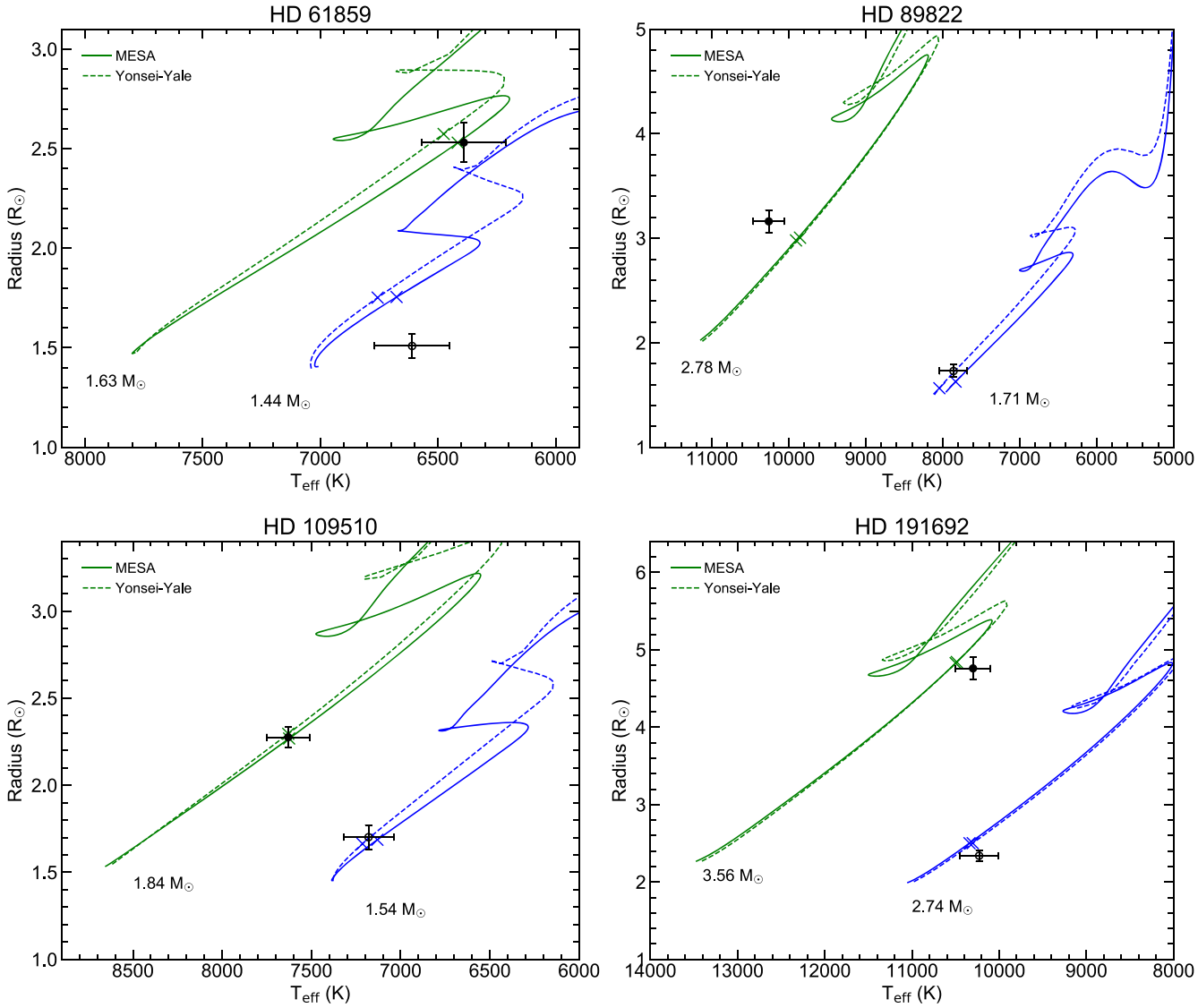

Figure 4. Evolutionary tracks for HD 61859 (top left), HD 89822 (top right), HD 109510 (bottom left), and HD 191692 (bottom right). The observed stellar parameters are shown as the filled points for the primary stars and open points for the secondary stars. The Yonsei–Yale models are shown as dashed lines and the MESA models are shown as solid lines, with green for the primary and blue for the secondary. The crosses represent the position of the mean system age on each track.

4.4. Comparison with Evolutionary Models

We created evolutionary tracks for the components of each binary system using the Yonsei–Yale (Demarque et al. 2004) and MESA (Paxton et al. 2011, 2019) codes in order to estimate the system ages and test the predictions of these models. We started with the observed masses and $\log Z/Z_{\odot}$ values from Table 3. The Yonsei–Yale models use a fixed overshooting parameter calculated from a step function in stellar mass. For the MESA models, we used the overshooting parameter ($f_{\rm ov}$) from the relation found by Claret & Torres (2018) and the default mixing length parameter of $\alpha_{\rm ov} = 2.0$, but adjusted $f_{\rm ov}$ and $\alpha_{\rm ov}$ slightly as needed to fit the observed parameters. Both models are nonrotating and use scaled Solar abundances.

Figure 4 shows the model evolutionary tracks and observed parameters of each binary system. For each component, we determined the age range where the model lies within the observed 1σ uncertainties. If the model lies outside the observed data point, we tried the 2σ uncertainties instead. If the component ages matched (to within 5%), we took a weighted average to estimate the binary system age, where the mean values corresponded to the best-fit age of each component and the uncertainties corresponded to the spread in possible ages. As described below, the component ages often did not match, so we adopted the primary star's age as the system age because it evolves faster and provides a tighter age constraint. The estimated binary ages are marked on each evolutionary track by a cross in Figure 4.

HD 61859—The Yonsei–Yale models match the observed parameters of the primary component at age of 1.90 Gyr near the end of the main sequence, but lie just outside the observed parameters of the secondary at an age of 1.50 Gyr. The MESA models match the observed parameters of the primary component at age of 1.60 Gyr, but lie just outside the observed parameters of the secondary at an age of 1.10 Gyr. The observed parameters of the primary are not consistent with either model at the age of the secondary, so we adopted the primary star's mean age of 1.75 Gyr as the age for the system.

A Solar-abundance evolutionary model would fit the secondary component better, despite being inconsistent with our spectroscopic analysis. Therefore, HD 61859 would benefit from a detailed abundance analysis to investigate whether or not the secondary component is chemically peculiar and solve this discrepancy.

HD 89822—The primary component is hotter and larger than predicted by both the Yonsei–Yale and MESA models. The closest position on the Yonsei–Yale tracks corresponds to 330 Myr, whereas the secondary component has an age of 510 Myr. The closest position on the MESA tracks corresponds to 300 Myr, whereas the secondary component has an age of 400 Myr. We adopted the primary star's mean age of 315 Myr for the system, because the primary star would be too evolved at the predicted ages of the secondary star. The primary component likely does not match the models because it is a HgMn star; its abundance anomalies could bias our temperature determination from Section 4.2 and our comparison to evolutionary models, because the BLUERED and MESA models both use scaled solar abundances. Because this system is quite young, we checked for membership in several nearby moving groups and associations using the BANYAN Σ tool (Gagné et al. 2018), but HD 89822 had a 99.9% chance of being a field star.

HD 109510—The Yonsei–Yale models successfully fit both components at an age of 1.04 Gyr, and the MESA models successfully fit both components at an age of 930 Myr using f_{ov} from Claret & Torres (2018) and the default α_{ov} parameter. Even though this system has large uncertainties in stellar mass, our results are likely still accurate because the component effective temperatures and radii fit quite well.

HD 191692—Both components of HD 191692 are slightly cooler and smaller than predicted by the Yonsei–Yale and MESA models. The primary component has evolved to the end of the main sequence; the closest model track point corresponds to an age of 220 Myr for the Yonsei–Yale models and 210 Myr for the MESA models. The closest track points to the secondary correspond to an age of 170 Myr for the Yonsei–Yale models and 190 Myr for the MESA models. Even though these are very close to the ages of the primary star, the primary evolves much faster and would only be halfway up the main sequence at these ages. Therefore, we adopt the primary star's mean age of 215 Myr as the estimated age of the binary. Note that Adelman et al. (2015) derived similar component effective temperatures from their abundance analysis, so perhaps the observed radii are underestimated and causing this age discrepancy. While the primary star is just barely resolved by our MIRC-X observations, its angular diameter would be well above the resolution limit at shorter wavelengths, so future interferometric observations would help solve this discrepancy between the observed and model parameters. Finally, we also checked if HD 191692 could be in young association using BANYAN Σ, but HD 191692 had a 99.9% chance of being a field star.

5. Discussion

We measured the visual and spectroscopic orbits for four binary systems using long baseline interferometry and high-resolution spectroscopy. We constrained the stellar masses to 1%–12% uncertainty, distances to 0.4%–6% uncertainty, and stellar radii to 3%–5% uncertainty. These fundamental parameters of longer period binaries ($P > 7$ days) are especially useful for testing our stellar models, because the component stars are less affected by tidal interactions and distortions and are better proxies for the evolution of single stars (Serenelli et al. 2021).

Typically, uncertainties in mass and radius less than 3% are needed to test our models of stellar structure and evolution (Torres et al. 2010). HD 61859 and HD 191692 meet this criterion for stellar mass, while additional observations with long baseline interferometry would be needed to more precisely measure the orbital inclinations and stellar masses of HD 89822 and HD 109510. HD 191692 also meets this criterion for stellar radius, because the primary's angular diameter was measured more precisely with the CHARA Array. We estimate that both components of HD 61859, the primary component of HD 89822, and both components of HD 191692 are resolvable with CHARA in visible light, so future work to measure directly the component radii would greatly improve the comparison with stellar evolution models.

We also found that HD 61859 is highly inclined and could create grazing eclipses. The TESS light curve potentially shows a very weak eclipse (0.1% depth) when the secondary star passes front of the primary star. However, no complementary eclipses were seen, and each TESS sector only covers two thirds of the binary orbit, so additional observations would be needed to confirm this system as an eclipsing binary.

Finally, the MESA models did not adequately fit the observed parameters of the chemically peculiar stars, HD 89822 and HD 191962, likely because their abundances are not scaled Solar values. Abt (1961) found that the metallic line phenomenon is linked to binarity, so further study of these systems could improve our understanding of the structure and evolution of HgMn and Am stars.

The authors would like to thank the staff at APO, CHARA, CTIO, and Fairborn Observatory for their invaluable support during observations. K.V.L. is supported by an appointment to the NASA Postdoctoral Program at the NASA Ames Research Center, administered by Oak Ridge Associated Universities under contract with NASA. This work is based upon observations obtained with the Apache Point Observatory 3.5 m telescope, owned and operated by the Astrophysical Research Consortium; the Georgia State University Center for High Angular Resolution Astronomy Array at Mount Wilson Observatory, supported by the National Science Foundation under grants Nos. AST-1636624, AST-1908026, and AST-2034336; and the CTIO/SMARTS 1.5 m telescope, operated as part of the SMARTS Consortium. Institutional support has been provided from the GSU College of Arts and Sciences and the GSU Office of the Vice President for Research and Economic Development. MIRC-X received funding from the European Research Council (ERC) under the European Union's Horizon 2020 research and innovation program (grant No. 639889). J.D.M. acknowledges funding for the development of MIRC-X (NASA-XRP NNX16AD43G, NSF-AST 1909165). S.K. acknowledges support from an ERC Consolidator Grant (Grant Agreement ID 101003096) and STFC Consolidated Grant (ST/V000721/1). Astronomy at Tennessee State University is supported by the state of Tennessee through its Centers of Excellence Program. This work has also made use of the Jean-Marie Mariotti Center Aspro &

SearchCal services, the CDS Astronomical Databases SIMBAD and VIZIER, the Wide-field Infrared Survey Explorer, and the Two Micron All Sky Survey.

Facilities: APO:3.5 m, CHARA, CTIO:1.5 m, TSU:AST.

Software: Grid Search for Binary Stars (Schaefer et al. 2016), MESA (Paxton et al. 2011), RVFIT (Iglesias-Marzoa et al. 2015), SearchCal (Chelli et al. 2016), TODCOR (Zucker & Mazeh 1994), Yonsei–Yale models (Demarque et al. 2004).

Appendix

We present our radial velocity measurements in Table 5, with the UT date, HJD date, radial velocity and uncertainty of each component, and the telescope used. We then list the calibrator stars' angular diameters in Table 6. Example plots of the final reconstructed spectra and best-fit model spectra are shown in Figures 5–8.

Table 5
Radial Velocity Measurements

Target	UT Date	HJD-2,400,000	$V_{r\,1}$ (km s^{-1})	σ_1 (km s^{-1})	$V_{r\,2}$ (km s^{-1})	σ_2 (km s^{-1})	Source
HD 61859	2011 Oct 06	55840.9727	−41.92	0.52	20.58	0.26	Fairborn
HD 61859	2011 Oct 15	55849.9297	18.28	0.52	−46.32	0.26	Fairborn
HD 61859	2011 Nov 23	55888.7539	24.98	0.52	−55.02	0.26	Fairborn
HD 61859	2012 Jan 01	55927.7266	−47.12	0.52	26.38	0.26	Fairborn
HD 61859	2012 Jan 18	55944.8945	21.68	0.52	−50.92	0.26	Fairborn
HD 61859	2012 Feb 25	55982.8242	29.28	0.52	−59.92	0.26	Fairborn
HD 61859	2012 Apr 04	56021.6875	−45.62	0.52	23.78	0.26	Fairborn
HD 61859	2012 May 13	56060.6953	−44.72	0.52	23.58	0.26	Fairborn
HD 61859	2012 Oct 16	56216.8750	−48.32	0.52	28.58	0.26	Fairborn
HD 61859	2012 Nov 04	56235.8281	19.58	0.52	−47.82	0.26	Fairborn
HD 61859	2012 Dec 17	56278.7109	−51.42	0.52	30.68	0.26	Fairborn
HD 61859	2013 Jan 05	56297.9297	28.18	0.52	−58.92	0.26	Fairborn
HD 61859	2013 Jan 16	56308.9297	−52.02	0.52	32.48	0.26	Fairborn
HD 61859	2013 Feb 01	56324.9414	35.28	0.52	−66.92	0.26	Fairborn
HD 61859	2013 Feb 17	56340.8398	−51.72	0.52	32.18	0.26	Fairborn
HD 61859	2013 Mar 24	56375.8242	−45.12	0.52	23.18	0.26	Fairborn
HD 61859	2013 Sep 21	56557.0156	−44.82	0.52	23.38	0.26	Fairborn
HD 61859	2013 Oct 11	56576.9414	36.18	0.52	−66.42	0.26	Fairborn
HD 61859	2013 Nov 26	56622.8594	−51.42	0.52	32.28	0.26	Fairborn
HD 61859	2013 Dec 16	56642.9688	39.18	0.52	−70.42	0.26	Fairborn
HD 61859	2014 Jan 01	56659.0195	−45.12	0.52	24.48	0.26	Fairborn
HD 61859	2014 Jan 17	56674.9531	36.18	0.52	−67.62	0.26	Fairborn
HD 61859	2014 Mar 17	56733.8281	31.18	0.52	−62.52	0.26	Fairborn
HD 61859	2014 Oct 28	56958.9648	32.78	0.52	−63.02	0.26	Fairborn
HD61859	2014 Dec 30	57021.9961	33.08	0.52	−63.02	0.26	Fairborn
HD 61859	2015 Feb 06	57059.9023	−37.52	0.52	15.68	0.26	Fairborn
HD 61859	2015 Oct 03	57298.9531	18.88	0.52	−46.62	0.26	Fairborn
HD 61859	2015 Nov 21	57347.8672	−52.42	0.52	32.68	0.26	Fairborn
HD 61859	2016 Jan 26	57413.6484	−48.41	0.49	28.79	0.34	APO
HD 61859	2016 Feb 11	57429.8359	40.78	0.52	−73.32	0.26	Fairborn
HD 61859	2016 Mar 15	57462.8203	33.78	0.52	−65.42	0.26	Fairborn
HD 61859	2016 Apr 14	57492.7852	41.18	0.52	−73.32	0.26	Fairborn
HD 61859	2016 May 10	57518.6641	12.28	0.52	−39.42	0.26	Fairborn
HD 61859	2016 Sep 16	57648.0078	36.18	0.52	−67.12	0.26	Fairborn
HD 61859	2016 Oct 16	57678.0000	26.18	0.52	−55.72	0.26	Fairborn
HD 61859	2017 Jan 26	57779.8008	13.48	0.52	−40.82	0.26	Fairborn
HD 61859	2017 Mar 09	57821.7266	−51.07	0.47	31.64	0.34	APO
HD 61859	2017 Mar 13	57825.7891	−41.22	0.52	18.28	0.26	Fairborn
HD 61859	2017 Apr 04	57847.6133	−38.00	0.46	17.10	0.33	APO
HD 61859	2017 Apr 13	57856.7305	−42.32	0.52	21.28	0.26	Fairborn
HD 61859	2017 May 27	57900.6562	39.48	0.52	−70.92	0.26	Fairborn
HD 61859	2017 Sep 18	58014.9219	−40.72	0.52	18.18	0.26	Fairborn
HD 61859	2017 Oct 30	58056.8828	31.88	0.52	−62.92	0.26	Fairborn
HD 61859	2017 Dec 02	58089.8438	38.59	0.48	−71.43	0.34	APO
HD 61859	2017 Dec 12	58099.8633	−40.52	0.52	19.08	0.26	Fairborn
HD 61859	2018 Jan 04	58122.6953	40.39	0.49	−72.88	0.35	APO
HD 61859	2018 Mar 19	58196.8555	−51.12	0.52	30.08	0.26	Fairborn
HD 61859	2018 Apr 04	58212.7109	18.65	0.45	−49.94	0.32	APO
HD 61859	2018 May 13	58251.7070	19.78	0.52	−49.82	0.26	Fairborn
HD 61859	2018 Oct 29	58420.9922	−50.82	0.52	30.48	0.26	Fairborn
HD 61859	2018 Nov 16	58438.7891	36.05	0.47	−69.16	0.34	APO
HD 61859	2018 Dec 24	58476.8945	−34.22	0.52	11.18	0.26	Fairborn
HD 61859	2019 Jan 14	58497.6406	29.80	0.48	−61.33	0.35	APO

Table 5
(Continued)

Target	UT Date	HJD-2,400,000	$V_{r\,1}$ (km s^{-1})	σ_1 (km s^{-1})	$V_{r\,2}$ (km s^{-1})	σ_2 (km s^{-1})	Source
HD 61859	2019 Jan 15	58498.7422	36.86	1.00	−67.55	0.72	APO
HD 61859	2019 Jan 19	58502.8945	28.35	0.44	−58.67	0.31	APO
HD 61859	2019 Jan 31	58514.9023	−51.08	0.48	30.98	0.34	APO
HD 61859	2019 Feb 25	58539.8281	−33.82	0.52	10.18	0.26	Fairborn
HD 61859	2019 Mar 24	58566.6914	19.95	0.44	−49.33	0.32	APO
HD 61859	2019 Oct 14	58770.9414	−39.27	0.48	17.66	0.35	APO
HD 61859	2019 Nov 13	58800.8242	−46.72	0.52	25.08	0.26	Fairborn
HD 61859	2019 Nov 14	58801.8203	−43.22	0.52	20.88	0.26	Fairborn
HD 61859	2019 Nov 14	58802.0078	−40.39	0.47	20.32	0.34	APO
HD 61859	2020 Jan 12	58860.7578	−50.79	0.46	32.45	0.32	APO
HD 61859	2020 Jan 12	58860.7891	−52.12	0.52	32.08	0.26	Fairborn
HD 61859	2020 Jan 27	58875.6953	30.88	0.52	−61.62	0.26	Fairborn
HD 61859	2020 Jan 28	58876.7081	37.08	0.52	−68.22	0.26	Fairborn
HD 61859	2020 Jan 29	58877.7080	41.58	0.52	−72.62	0.26	Fairborn
HD 61859	2020 Jan 31	58879.7079	37.98	0.52	−69.22	0.26	Fairborn
HD 61859	2020 Feb 01	58880.7079	30.08	0.52	−61.42	0.26	Fairborn
HD 61859	2020 Feb 02	58881.7079	20.68	0.52	−49.32	0.26	Fairborn
HD 61859	2020 Feb 07	58886.7077	−36.22	0.52	13.48	0.26	Fairborn
HD 61859	2020 Feb 08	58887.7077	−42.52	0.52	21.18	0.26	Fairborn
HD 61859	2020 Feb 09	58888.7076	−47.02	0.52	26.28	0.26	Fairborn
HD 61859	2020 Feb 14	58893.7074	−49.92	0.52	29.98	0.26	Fairborn
HD 61859	2020 Feb 14	58893.7539	−49.11	0.46	29.98	0.32	APO
HD 89822	2005 Feb 09	53410.8867	12.20	0.22	−25.17	0.49	Fairborn
HD 89822	2005 Apr 01	53461.8945	−21.91	0.22	29.61	0.49	Fairborn
HD 89822	2005 Apr 16	53476.8242	22.87	0.22	−43.30	0.49	Fairborn
HD 89822	2005 May 05	53495.9180	−39.67	0.22	60.16	0.49	Fairborn
HD 89822	2005 May 21	53511.8711	23.34	0.22	−43.76	0.49	Fairborn
HD 89822	2006 Jan 31	53766.8867	24.40	0.22	−46.04	0.49	Fairborn
HD 89822	2006 Apr 17	53842.8672	−48.70	0.22	73.82	0.49	Fairborn
HD 89822	2006 May 14	53869.8242	19.00	0.22	−36.81	0.49	Fairborn
HD 89822	2006 May 30	53885.7500	10.52	0.22	−21.62	0.49	Fairborn
HD 89822	2017 Jan 11	57764.8320	9.09	0.53	−20.18	1.54	APO
HD 89822	2017 Feb 16	57800.8867	−16.10	0.51	22.17	1.56	APO
HD 89822	2017 Mar 09	57821.7422	18.95	0.55	−36.05	1.64	APO
HD 89822	2017 Apr 04	57847.6406	−28.27	0.54	40.76	1.62	APO
HD 89822	2017 Apr 10	57853.6602	22.15	0.71	−41.97	2.13	APO
HD 89822	2017 Dec 27	58114.7695	−47.77	0.68	73.27	2.00	APO
HD 89822	2018 Jan 04	58122.7500	18.62	0.55	−37.10	1.61	APO
HD 89822	2018 Jan 28	58146.9023	9.31	0.50	−21.46	1.47	APO
HD 89822	2018 Apr 04	58212.7305	22.88	0.53	−42.29	1.56	APO
HD 89822	2019 Jan 19	58502.9492	24.84	0.50	−44.53	1.48	APO
HD 89822	2019 Jan 22	58505.7930	9.71	0.53	−23.13	1.57	APO
HD 89822	2019 Jan 31	58514.9141	24.61	0.52	−44.97	1.51	APO
HD 89822	2019 Feb 17	58531.6211	−48.14	0.57	72.88	1.66	APO
HD 89822	2019 Mar 24	58566.7266	−51.54	0.56	78.12	1.66	APO
HD 89822	2019 Apr 21	58594.8203	22.62	0.22	−43.11	0.49	Fairborn
HD 89822	2019 Apr 26	58599.9062	−18.51	0.22	24.87	0.49	Fairborn
HD 89822	2019 Apr 27	58600.7969	−42.11	0.22	62.64	0.49	Fairborn
HD 89822	2019 May 02	58605.8711	20.06	0.22	−38.11	0.49	Fairborn
HD 89822	2019 May 04	58607.7891	24.41	0.22	−45.97	0.49	Fairborn
HD 89822	2019 May 18	58621.6367	9.95	0.22	−20.78	0.49	Fairborn
HD 89822	2019 Jun 05	58639.7500	13.34	0.22	−27.28	0.49	Fairborn
HD 89822	2019 Jun 19	58653.8320	24.66	0.22	−45.41	0.49	Fairborn
HD 89822	2019 Jun 20	58654.7461	22.74	0.22	−43.04	0.49	Fairborn
HD 89822	2019 Jun 21	58655.7578	16.49	0.22	−32.00	0.49	Fairborn
HD 89822	2019 Jun 23	58657.7148	−15.73	0.22	20.75	0.49	Fairborn
HD 89822	2019 Jun 24	58658.7422	−43.53	0.22	64.73	0.49	Fairborn
HD 89822	2019 Jun 25	58659.7188	−49.77	0.22	75.39	0.49	Fairborn
HD 89822	2019 Jun 26	58660.6758	−27.83	0.22	39.81	0.49	Fairborn
HD 89822	2019 Sep 19	58745.9727	24.25	0.22	−45.99	0.49	Fairborn
HD 89822	2019 Oct 05	58761.9141	−15.83	0.22	19.91	0.49	Fairborn
HD 89822	2019 Oct 06	58762.9219	−42.92	0.22	63.11	0.49	Fairborn

Table 5
(Continued)

Target	UT Date	HJD-2,400,000	$V_{r\,1}$ (km s^{-1})	σ_1 (km s^{-1})	$V_{r\,2}$ (km s^{-1})	σ_2 (km s^{-1})	Source
HD 89822	2019 Oct 07	58763.9375	−49.41	0.22	73.76	0.49	Fairborn
HD 89822	2019 Oct 08	58764.9336	−27.03	0.22	38.61	0.49	Fairborn
HD 89822	2019 Oct 14	58770.9844	19.99	0.59	−39.24	1.79	APO
HD 89822	2019 Oct 19	58776.0352	−39.42	0.22	58.53	0.49	Fairborn
HD 89822	2019 Oct 20	58776.9180	−16.82	0.22	21.10	0.49	Fairborn
HD 89822	2019 Oct 24	58781.0391	24.53	0.22	−46.57	0.49	Fairborn
HD 89822	2019 Oct 25	58782.0391	23.18	0.22	−44.21	0.49	Fairborn
HD 89822	2019 Oct 26	58782.8672	18.71	0.22	−35.75	0.49	Fairborn
HD 89822	2019 Oct 30	58786.8555	−51.43	0.22	77.33	0.49	Fairborn
HD 89822	2019 Oct 31	58787.7812	−35.30	0.22	51.06	0.49	Fairborn
HD 89822	2019 Nov 14	58802.0273	14.94	0.54	−29.78	1.57	APO
HD 89822	2019 Nov 23	58810.8086	−38.71	0.22	56.24	0.49	Fairborn
HD 89822	2019 Dec 17	58834.7422	−18.47	0.22	23.21	0.49	Fairborn
HD 89822	2019 Dec 20	58837.7500	22.06	0.22	−42.07	0.49	Fairborn
HD 89822	2019 Dec 21	58838.7891	24.70	0.22	−46.26	0.49	Fairborn
HD 89822	2020 Jan 08	58856.7891	−46.02	0.22	68.84	0.49	Fairborn
HD 89822	2020 Jan 12	58860.7734	20.97	0.53	−39.66	1.63	APO
HD 89822	2020 Jan 18	58866.9258	−37.62	0.22	55.50	0.49	Fairborn
HD 89822	2020 Jan 19	58867.9258	−51.66	0.22	77.62	0.49	Fairborn
HD 89822	2020 Jan 31	58879.6992	−49.89	0.22	75.10	0.49	Fairborn
HD 89822	2020 Feb 08	58887.6992	12.78	0.22	−26.24	0.49	Fairborn
HD 89822	2020 Feb 15	58894.8906	16.63	0.22	−33.77	0.49	Fairborn
HD 89822	2020 Feb 16	58895.6484	21.51	0.22	−41.46	0.49	Fairborn
HD 89822	2020 Feb 17	58896.6367	24.57	0.22	−46.32	0.49	Fairborn
HD 89822	2020 Feb 18	58897.6406	23.60	0.22	−44.93	0.49	Fairborn
HD 89822	2020 Feb 19	58898.8320	17.00	0.22	−33.39	0.49	Fairborn
HD 109510	2017 Feb 16	57800.9109	54.17	0.43	−55.91	1.19	APO
HD 109510	2017 Mar 09	57821.7621	78.15	0.46	−85.41	1.26	APO
HD 109510	2017 Dec 02	58089.9622	−46.53	0.48	62.37	1.31	APO
HD 109510	2018 May 10	58248.5463	49.63	0.15	−51.71	1.09	CTIO
HD 109510	2019 Jan 13	58496.8454	80.35	0.18	−88.34	0.53	CTIO
HD 109510	2019 Jan 16	58499.8734	−22.54	0.17	34.88	0.49	CTIO
HD 109510	2019 Jan 17	58500.8871	−47.58	0.18	63.47	0.51	CTIO
HD 109510	2019 Jan 28	58511.8517	78.76	0.19	−86.67	0.54	CTIO
HD 109510	2019 Jan 29	58512.8259	42.81	0.19	−43.54	0.56	CTIO
HD 109510	2019 Jan 31	58514.9867	−34.64	0.45	49.45	1.18	APO
HD 109510	2019 Feb 12	58526.8152	70.69	0.20	−76.22	0.56	CTIO
HD 109510	2019 Feb 13	58527.8282	28.73	0.18	−26.07	0.50	CTIO
HD 109510	2019 Feb 15	58529.8156	−38.68	0.18	53.55	0.49	CTIO
HD 109510	2019 Feb 16	58530.8338	−54.88	0.18	72.77	0.53	CTIO
HD 109510	2019 Feb 17	58531.7947	−40.67	0.18	55.52	0.51	CTIO
HD 109510	2019 Feb 18	58532.8140	39.66	0.17	−39.42	0.51	CTIO
HD 109510	2019 Feb 24	58538.8251	−50.32	0.19	67.04	0.55	CTIO
HD 109510	2019 Feb 26	58540.7412	77.76	0.19	−85.32	0.53	CTIO
HD 109510	2019 Feb 27	58541.7464	60.88	0.18	−64.90	0.52	CTIO
HD 109510	2019 Mar 05	58547.7628	62.38	0.17	−66.44	0.48	CTIO
HD 109510	2019 Mar 21	58563.7068	62.93	0.10	−66.97	0.77	CTIO
HD 109510	2019 Mar 21	58563.7323	62.15	0.17	−66.21	0.49	CTIO
HD 109510	2019 Mar 24	58566.7556	−44.78	0.46	60.14	1.25	APO
HD 109510	2019 Mar 27	58569.7259	58.93	0.18	−62.56	0.49	CTIO
HD 109510	2019 Nov 14	58802.0294	−52.61	0.48	69.84	1.30	APO
HD 109510	2020 Jan 07	58855.8570	59.03	0.19	−62.26	0.53	CTIO
HD 109510	2020 Jan 08	58856.8712	73.88	0.20	−79.82	0.56	CTIO
HD 109510	2020 Jan 14	58862.8429	28.21	0.18	−25.05	0.50	CTIO
HD 109510	2020 Jan 15	58863.8831	80.80	0.18	−88.49	0.52	CTIO
HD 109510	2020 Jan 16	58864.8731	47.75	0.18	−49.18	0.52	CTIO
HD 109510	2020 Jan 19	58867.8896	−50.26	0.42	66.74	1.25	CTIO
HD 109510	2020 Jan 20	58868.8921	−51.79	0.20	68.98	0.59	CTIO
HD 109510	2020 Jan 23	58871.8459	63.04	0.20	−66.87	0.54	CTIO
HD 109510	2020 Jan 26	58874.8406	−43.16	0.44	59.32	1.25	CTIO
HD 109510	2020 Jan 28	58876.8490	−28.61	0.22	42.62	0.64	CTIO
HD 109510	2020 Jan 29	58877.8545	58.01	0.55	−61.83	1.60	CTIO
HD 109510	2020 Jan 31	58879.8639	34.24	0.19	−32.34	0.54	CTIO

Table 5
(Continued)

Target	UT Date	HJD-2,400,000	$V_{r\,1}$ (km s^{-1})	σ_1 (km s^{-1})	$V_{r\,2}$ (km s^{-1})	σ_2 (km s^{-1})	Source
HD 109510	2020 Feb 14	58893.7607	65.90	0.47	−71.83	1.27	APO
HD 109510	2020 Feb 25	58904.8786	−53.80	0.25	72.06	0.28	Fairborn
HD 109510	2020 May 07	58976.8105	−24.13	0.25	36.26	0.28	Fairborn
HD 109510	2020 Dec 21	59204.8936	−40.80	0.25	57.10	0.28	Fairborn
HD 109510	2021 Jan 04	59218.8653	−22.15	0.25	34.62	0.28	Fairborn
HD 109510	2021 Jan 14	59228.8270	−38.18	0.25	53.64	0.28	Fairborn
HD 109510	2021 Feb 06	59251.9700	53.97	0.25	−56.89	0.28	Fairborn
HD 109510	2021 Feb 23	59268.7125	33.74	0.25	−32.85	0.28	Fairborn
HD 109510	2021 Mar 15	59288.9302	72.45	0.25	−78.32	0.28	Fairborn
HD 109510	2021 Mar 20	59293.9990	−55.02	0.25	73.54	0.28	Fairborn
HD 109510	2021 Mar 31	59304.8677	56.47	0.25	−60.25	0.28	Fairborn
HD 109510	2021 Apr 10	59314.9131	−40.57	0.25	56.27	0.28	Fairborn
HD 109510	2021 Apr 18	59322.8794	−51.72	0.25	69.37	0.28	Fairborn
HD 109510	2021 Apr 30	59334.8455	29.79	0.25	−27.46	0.28	Fairborn
HD 109510	2021 May 04	59338.6809	−45.86	0.25	62.51	0.28	Fairborn
HD 109510	2021 May 05	59339.6808	23.70	0.25	−19.79	0.28	Fairborn
HD 109510	2021 May 06	59340.6808	81.24	0.25	−89.27	0.28	Fairborn
HD 109510	2021 May 07	59341.6807	51.46	0.25	−53.23	0.28	Fairborn
HD 109510	2021 May 09	59343.6806	−25.46	0.25	37.79	0.28	Fairborn
HD 109510	2021 May 10	59344.6804	−48.69	0.25	65.92	0.28	Fairborn
HD 109510	2021 May 11	59345.6804	−53.12	0.25	71.12	0.28	Fairborn
HD 109510	2021 May 13	59347.6803	74.44	0.25	−81.92	0.28	Fairborn
HD 109510	2021 May 14	59348.6802	65.22	0.25	−69.70	0.28	Fairborn
HD 109510	2021 May 15	59349.6801	22.51	0.25	−19.40	0.28	Fairborn
HD 109510	2021 May 16	59350.6800	−14.75	0.25	25.09	0.28	Fairborn
HD 109510	2021 May 17	59351.6800	−42.78	0.25	57.94	0.28	Fairborn
HD 109510	2021 May 18	59352.6799	−55.24	0.25	73.34	0.28	Fairborn
HD 109510	2021 May 19	59353.6798	−31.78	0.25	45.14	0.28	Fairborn
HD 109510	2021 May 24	59358.6794	−34.06	0.25	48.42	0.28	Fairborn
HD 109510	2021 May 25	59359.6793	−53.45	0.25	71.30	0.28	Fairborn
HD 109510	2021 May 26	59360.6793	−46.53	0.25	62.81	0.28	Fairborn
HD 109510	2021 May 28	59362.6791	81.34	0.25	−89.00	0.28	Fairborn
HD 109510	2021 May 29	59363.6790	51.51	0.25	−54.07	0.28	Fairborn
HD 191692	2004 Mar 27	53091.9720	29.60	0.89	−101.50	1.79	Fairborn
HD 191692	2004 Oct 05	53283.7036	−47.10	1.34	−0.70	2.68	Fairborn
HD 191692	2004 Oct 18	53296.6486	4.80	0.89	−74.40	1.79	Fairborn
HD 191692	2004 Oct 24	53302.7319	−53.60	1.34	3.70	2.68	Fairborn
HD 191692	2004 Oct 25	53303.6305	−53.70	1.34	3.70	2.68	Fairborn
HD 191692	2004 Nov 05	53314.6562	28.80	0.89	−101.90	1.79	Fairborn
HD 191692	2004 Nov 11	53320.6595	−52.60	1.34	4.50	2.68	Fairborn
HD 191692	2014 Jul 03	56841.8663	17.37	0.24	−90.68	0.36	CTIO
HD 191692	2019 Jun 06	58640.8262	43.15	0.32	−123.37	0.46	CTIO
HD 191692	2019 Aug 12	58707.6604	0.24	0.25	−68.29	0.38	CTIO
HD 191692	2019 Aug 13	58708.6722	25.08	0.30	−100.51	0.45	CTIO
HD 191692	2019 Aug 14	58709.6792	39.63	0.36	−119.35	0.51	CTIO
HD 191692	2019 Aug 17	58712.6434	−51.92	0.45	0.28	0.60	CTIO
HD 191692	2019 Aug 29	58724.6105	−2.38	0.25	−64.37	0.37	CTIO
HD 191692	2019 Aug 30	58725.6912	21.91	0.28	−96.19	0.41	CTIO
HD 191692	2019 Aug 31	58726.5889	43.76	0.27	−124.37	0.39	CTIO
HD 191692	2019 Sep 03	58729.6022	−50.62	0.42	−0.36	0.54	CTIO
HD 191692	2019 Sep 04	58730.5631	−53.58	0.42	2.39	0.57	CTIO
HD 191692	2019 Sep 05	58731.5943	−53.72	0.46	2.28	0.63	CTIO
HD 191692	2019 Sep 15	58741.5586	−5.50	0.27	−60.96	0.37	CTIO
HD 191692	2019 Sep 16	58742.5689	14.65	0.26	−87.40	0.38	CTIO
HD 191692	2019 Sep 17	58743.5649	42.85	0.33	−123.43	0.47	CTIO
HD 191692	2019 Oct 05	58761.6219	3.61	0.28	−72.76	0.41	CTIO
HD 191692	2019 Oct 10	58766.5178	−52.65	0.45	0.97	0.62	CTIO
HD 191692	2019 Oct 10	58766.6965	−54.20	1.34	−1.20	2.68	Fairborn
HD 191692	2019 Oct 10	58767.4814	−50.46	0.61	−0.37	0.78	CTIO
HD 191692	2019 Oct 11	58767.5990	−52.20	1.34	−0.60	2.68	Fairborn
HD 191692	2019 Oct 19	58775.6700	−6.00	0.89	−57.60	1.79	Fairborn
HD 191692	2019 Oct 20	58776.5546	8.29	0.47	−79.32	0.70	CTIO

Table 5
(Continued)

Target	UT Date	HJD-2,400,000	$V_{r\,1}$ (km s^{-1})	σ_1 (km s^{-1})	$V_{r\,2}$ (km s^{-1})	σ_2 (km s^{-1})	Source
HD 191692	2019 Oct 20	58776.6822	12.50	0.89	−82.40	1.79	Fairborn
HD 191692	2019 Oct 21	58777.5640	37.04	0.32	−116.10	0.47	CTIO
HD 191692	2019 Oct 21	58777.6927	39.70	0.89	−121.60	1.79	Fairborn
HD 191692	2019 Oct 22	58778.5228	19.41	0.31	−92.89	0.44	CTIO
HD 191692	2019 Oct 22	58778.6162	11.90	0.89	−83.00	1.79	Fairborn
HD 191692	2019 Oct 25	58781.5327	−52.55	0.44	1.49	0.60	CTIO
HD 191692	2019 Oct 26	58782.6390	−54.40	1.34	1.70	2.68	Fairborn
HD 191692	2019 Oct 27	58783.6384	−53.70	1.34	2.50	2.68	Fairborn
HD 191692	2019 Nov 06	58793.5064	4.57	0.29	−74.38	0.44	CTIO
HD 191692	2019 Nov 07	58795.4940	29.78	0.31	−106.24	0.45	CTIO
HD 191692	2020 Sep 11	59103.6197	36.50	0.89	−115.20	1.79	Fairborn
HD 191692	2020 Sep 16	59108.6166	−56.10	1.34	4.50	2.68	Fairborn
HD 191692	2020 Sep 17	59109.6126	−52.20	1.34	2.70	2.68	Fairborn
HD 191692	2020 Sep 25	59117.6385	−13.30	0.89	−50.00	1.79	Fairborn
HD 191692	2020 Sep 26	59118.6016	1.50	0.89	−67.30	1.79	Fairborn
HD 191692	2020 Sep 27	59119.6038	25.20	0.89	−95.50	1.79	Fairborn
HD 191692	2020 Sep 28	59120.6023	41.70	0.89	−125.10	1.79	Fairborn
HD 191692	2020 Sep 29	59121.6015	−17.60	0.89	−44.60	1.79	Fairborn
HD 191692	2020 Sep 30	59122.6014	−44.50	1.34	−8.00	2.68	Fairborn
HD 191692	2020 Oct 01	59123.6002	−53.10	1.34	−0.20	2.68	Fairborn
HD 191692	2020 Oct 02	59124.5996	−54.30	1.34	3.60	2.68	Fairborn
HD 191692	2020 Oct 03	59125.5985	−54.80	1.34	3.10	2.68	Fairborn
HD 191692	2020 Oct 04	59126.5986	−53.50	1.34	2.10	2.68	Fairborn
HD 191692	2020 Oct 05	59127.5947	−50.10	1.34	−1.20	2.68	Fairborn
HD 191692	2020 Oct 06	59128.5935	−47.90	1.34	−4.30	2.68	Fairborn
HD 191692	2020 Oct 13	59135.6121	−1.70	0.89	−64.30	1.79	Fairborn
HD 191692	2020 Oct 14	59136.5880	19.80	0.89	−90.60	1.79	Fairborn
HD 191692	2020 Oct 15	59137.5874	44.40	0.89	−127.00	1.79	Fairborn
HD 191692	2020 Oct 16	59138.5866	−9.80	0.89	−52.00	1.79	Fairborn
HD 191692	2020 Oct 18	59140.5850	−52.90	1.34	0.80	2.68	Fairborn
HD 191692	2020 Oct 19	59141.5841	−52.90	1.34	3.40	2.68	Fairborn
HD 191692	2020 Oct 20	59142.6096	−53.10	1.34	3.40	2.68	Fairborn
HD 191692	2020 Oct 21	59143.6136	−53.60	1.34	2.30	2.68	Fairborn
HD 191692	2020 Oct 22	59144.6130	−50.60	1.34	−1.00	2.68	Fairborn
HD 191692	2020 Oct 30	59152.6153	−2.70	0.89	−61.10	1.79	Fairborn
HD 191692	2020 Oct 31	59153.6148	17.40	0.89	−88.10	1.79	Fairborn
HD 191692	2020 Nov 01	59154.6248	44.20	0.89	−125.90	1.79	Fairborn
HD 191692	2020 Nov 02	59155.6256	−4.50	0.89	−58.50	1.79	Fairborn
HD 191692	2020 Nov 04	59157.6228	−52.50	1.34	0.50	2.68	Fairborn
HD 191692	2020 Nov 05	59158.6216	−53.80	1.34	3.10	2.68	Fairborn
HD 191692	2020 Nov 17	59170.6104	13.40	0.89	−83.00	1.79	Fairborn
HD 191692	2020 Nov 18	59171.6560	43.50	0.89	−127.20	1.79	Fairborn
HD 191692	2020 Nov 19	59172.6341	4.00	0.89	−69.90	1.79	Fairborn
HD 191692	2020 Nov 21	59174.6069	−51.50	1.34	−1.90	2.68	Fairborn
HD 191692	2020 Nov 22	59175.6065	−54.00	1.34	5.20	2.68	Fairborn
HD 191692	2020 Nov 25	59178.6170	−51.50	1.34	0.70	2.68	Fairborn
HD 191692	2021 Feb 12	59258.0383	17.70	0.89	−92.90	1.79	Fairborn
HD 191692	2021 Feb 28	59274.0231	32.70	0.89	−109.50	1.79	Fairborn
HD 191692	2021 Mar 01	59275.0178	26.70	0.89	−102.80	1.79	Fairborn
HD 191692	2021 Apr 09	59314.0086	−54.40	1.34	2.40	2.68	Fairborn
HD 191692	2021 Apr 20	59324.8890	18.10	0.89	−90.00	1.79	Fairborn
HD 191692	2021 Apr 24	59328.8698	−52.20	1.34	0.20	2.68	Fairborn
HD 191692	2021 May 07	59341.8248	12.30	0.89	−82.30	1.79	Fairborn
HD 191692	2021 Jun 01	59366.8105	−52.70	1.34	−1.20	2.68	Fairborn

Table 6
Calibrator Angular Diameters

Target	Calibrator	θ_{UD} (mas)	Wavelength
HD 61859	HD 45391	0.329 ± 0.017	*H*-band
HD 61859	HD 56124	0.346 ± 0.008	*K*-band
HD 61859	HD 59037	0.391 ± 0.011	*K*-band
HD 61859	HD 59747	0.348 ± 0.017	*K*-band
HD 61859	HD 63495	0.122 ± 0.006	*K*-band
HD 61859	HD 67709	0.443 ± 0.010	*K*-band
HD 61859	HD 67827	0.387 ± 0.019	*K*-band
HD 61859	HD 72524	0.256 ± 0.013	*H*-band
HD 89822	HD 84812	0.300 ± 0.015	*H*-band
HD 89822	HD 88983	0.313 ± 0.008	*K*-band
HD 89822	HD 96707	0.296 ± 0.007	*K*-band
HD 89822	HD 98772	0.235 ± 0.012	*H*-band
HD 109510	HD 105086	0.319 ± 0.016	*H*-band
HD 109510	HD 107569	0.242 ± 0.006	*K*-band
HD 109510	HD 111718	0.231 ± 0.005	*K*-band
HD 109510	HD 111893	0.263 ± 0.013	*H*-band
HD 191692	HD 188350	0.284 ± 0.008	*K*-band
HD 191692	HD 191014	0.826 ± 0.073	*K*-band
HD 191692	HD 193329	0.831 ± 0.082	*K*-band
HD 191692	HD 195810	0.323 ± 0.029	*K*-band
HD 191692	HD 185124	0.495 ± 0.025	*H*-band
HD 191692	HD 196870	0.661 ± 0.050	*H*-band

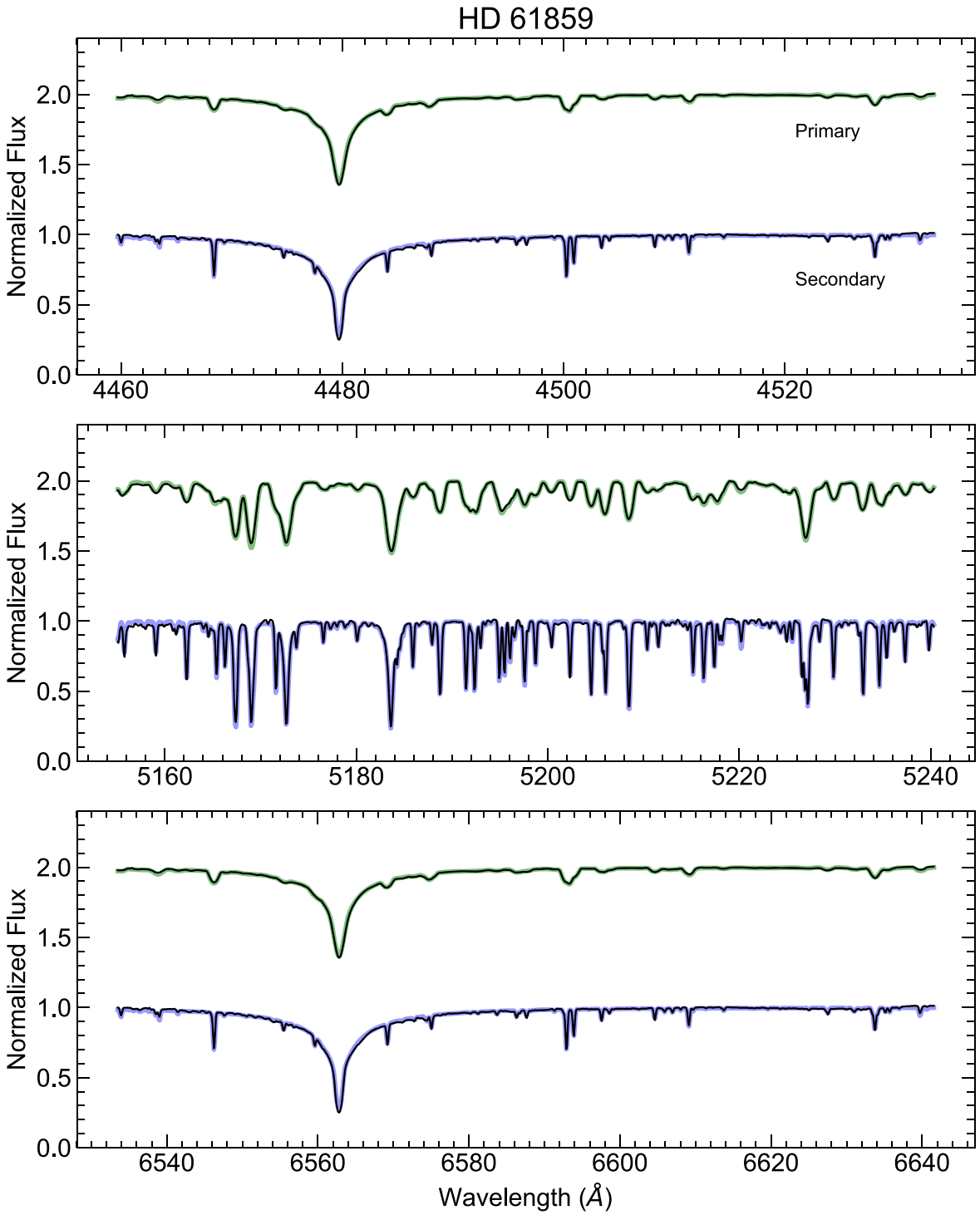

Figure 5. Reconstructed spectra of HD 61859 around Hβ (top), the Mg b triplet (middle), and Hα (bottom), for example. The reconstructed spectra are shown in black, and the best-fit model spectra are overplotted in green for the primary and blue for the secondary.

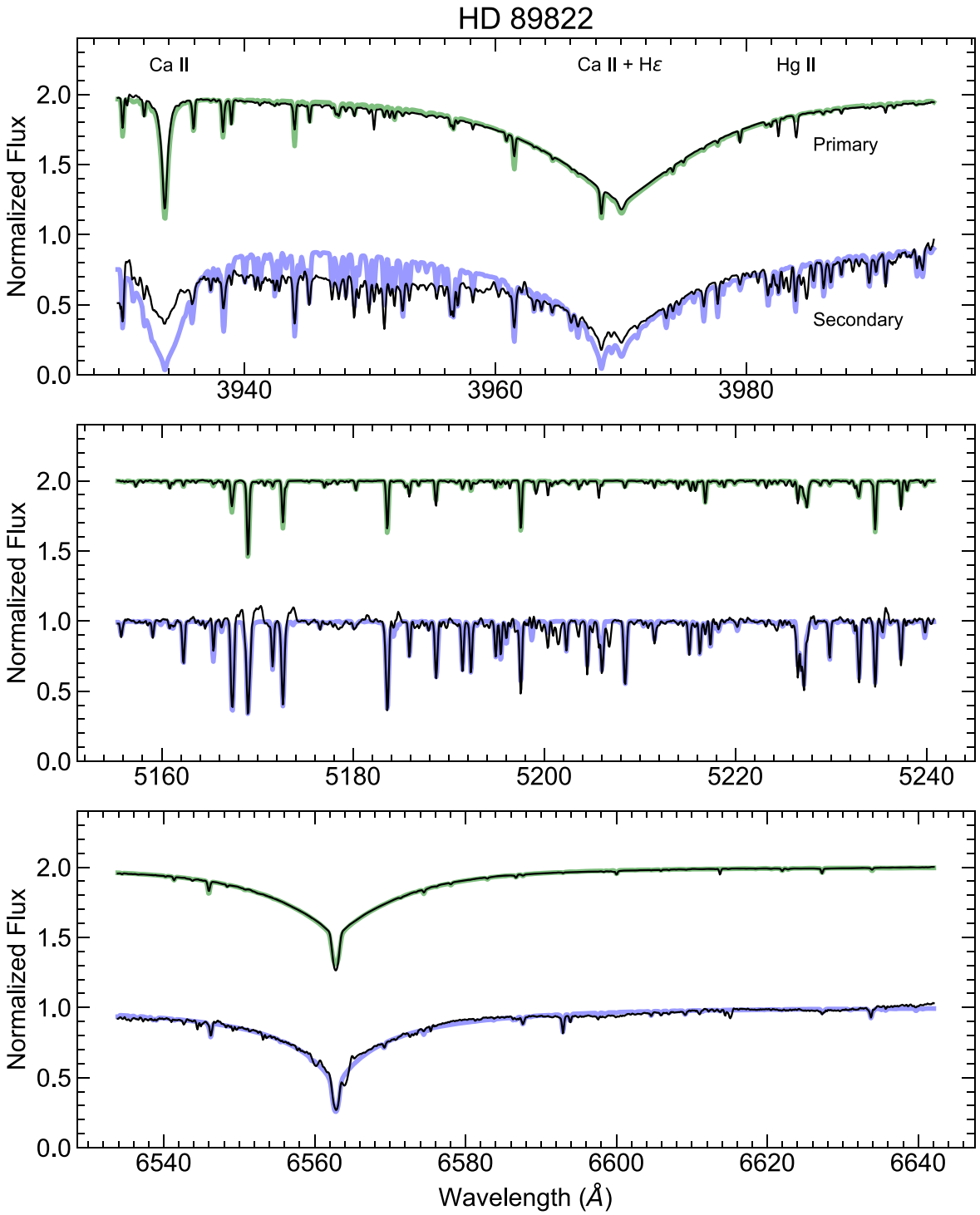

Figure 6. Reconstructed spectra of HD 89822 around the Ca H & K lines (top), the Mg b triplet (middle), and Hα (bottom), for example. The reconstructed spectra are shown in black, and the best-fit model spectra are overplotted in green for the primary and blue for the secondary. In the top panel, lines relevant to HgMn and Am stars are labeled, including Ca K 3934 Å, a blend of Ca H 3969 Å with Hϵ 3970 Å, and Hg II 3984 Å. The Hg II line is much stronger in the primary star than in the models as expected for HgMn stars, and the Ca K line of the secondary component is much weaker than in the models as expected for metallic line stars.

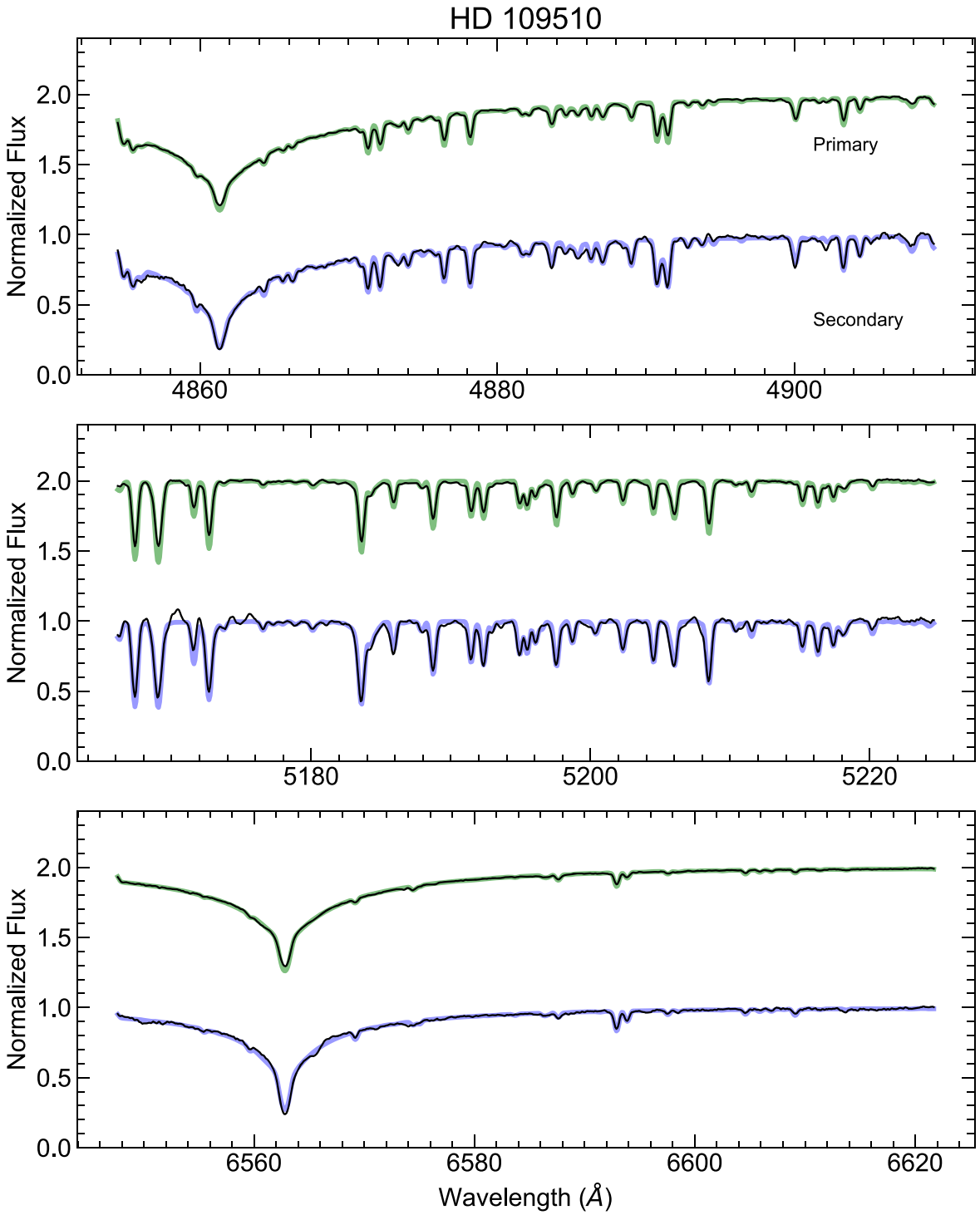

Figure 7. Reconstructed spectra of HD 109510 around Hβ (top), the Mg b triplet (middle), and Hα (bottom), for example. The reconstructed spectra are shown in black, and the best-fit model spectra are overplotted in green for the primary and blue for the secondary.

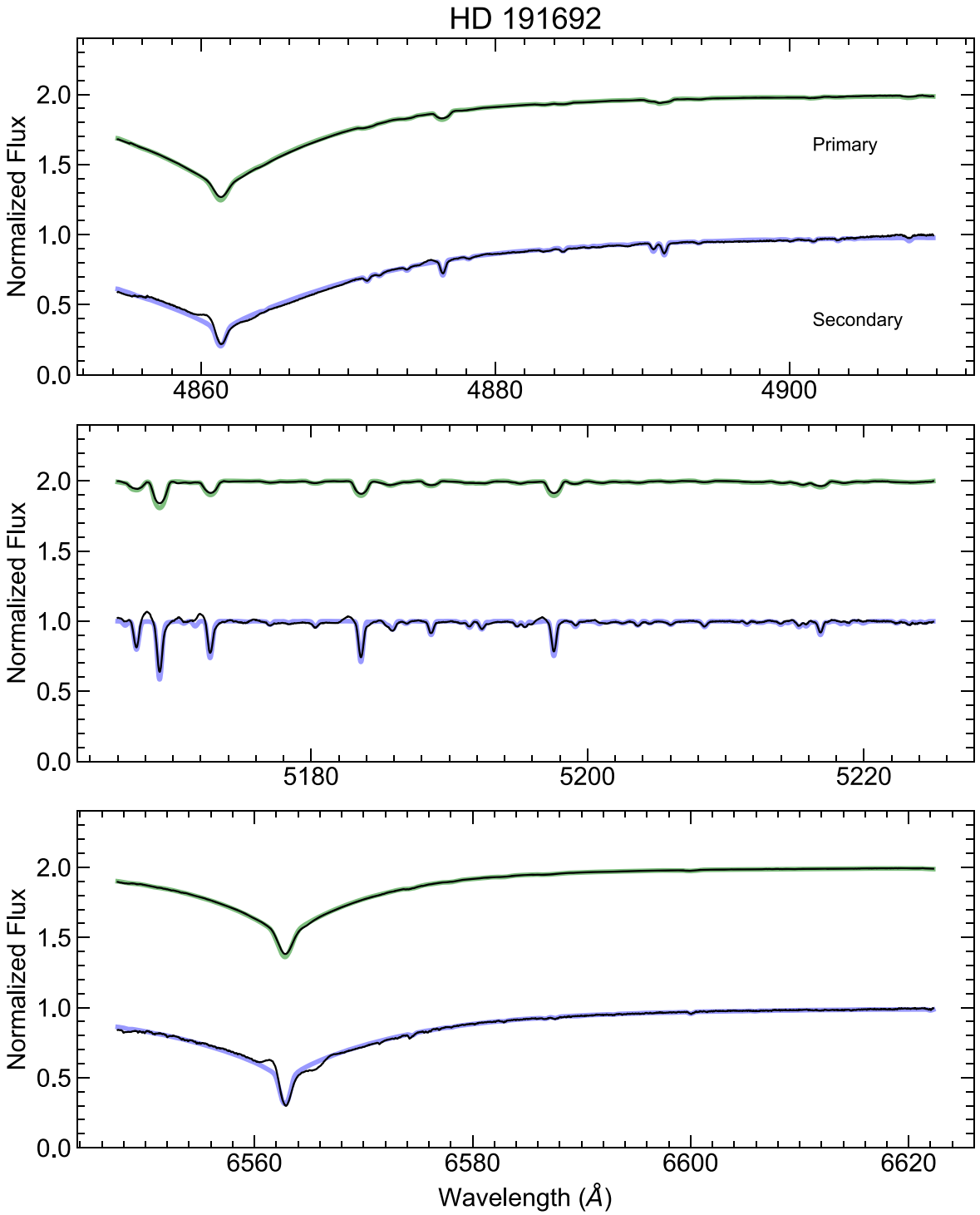

Figure 8. Reconstructed spectra of HD 191692 around Hβ (top), the Mg b triplet (middle), and Hα (bottom), for example. The reconstructed spectra are shown in black, and the best-fit model spectra are overplotted in green for the primary and blue for the secondary.

ORCID iDs

Kathryn V. Lester https://orcid.org/0000-0002-9903-9911
Gail H. Schaefer https://orcid.org/0000-0001-5415-9189
Francis C. Fekel https://orcid.org/0000-0002-9413-3896
Douglas R. Gies https://orcid.org/0000-0001-8537-3583
Todd J. Henry https://orcid.org/0000-0002-9061-2865
Wei-Chun Jao https://orcid.org/0000-0003-0193-2187
Leonardo A. Paredes https://orcid.org/0000-0003-1324-0495
Hodari-Sadiki Hubbard-James https://orcid.org/0000-0003-4568-2079
Christopher D. Farrington https://orcid.org/0000-0001-9939-2830
Kathryn D. Gordon https://orcid.org/0000-0003-1338-531X
S. Drew Chojnowski https://orcid.org/0000-0001-9984-0891
John D. Monnier https://orcid.org/0000-0002-3380-3307
Stefan Kraus https://orcid.org/0000-0001-6017-8773

Jean-Baptiste Le Bouquin https://orcid.org/0000-0002-0493-4674
Narsireddy Anugu https://orcid.org/0000-0002-2208-6541
Theo Ten Brummelaar https://orcid.org/0000-0002-0114-7915
Claire L. Davies https://orcid.org/0000-0001-9764-2357
Tyler Gardner https://orcid.org/0000-0002-3003-3183
Aaron Labdon https://orcid.org/0000-0001-8837-7045
Cyprien Lanthermann https://orcid.org/0000-0001-9745-5834
Benjamin R. Setterholm https://orcid.org/0000-0001-5980-0246

References

Abt, H. A. 1961, ApJS, 6, 37
Abt, H. A., & Snowden, M. S. 1973, ApJS, 25, 137
Adelman, S. J. 1994, MNRAS, 266, 97
Adelman, S. J., Yüce, K., & Gulliver, A. F. 2015, PASP, 127, 509
Anugu, N., Le Bouquin, J.-B., Monnier, J. D., et al. 2020, AJ, 160, 158
Bagnuolo, W. G., Jr., Gies, D. R., & Wiggs, M. S. 1992, ApJ, 385, 708
Bertone, E., Buzzoni, A., Chávez, M., & Rodríguez-Merino, L. H. 2008, A&A, 485, 823
Bordier, E., Frost, A. J., Sana, H., et al. 2022, A&A, 663, A26
Burnashev, V. I. 1985, AbaOB, 59, 83
Castelli, F., & Kurucz, R. L. 2004, in IAU Symp. 210, Modelling of Stellar Atmospheres, ed. N. Piskunov, W. W. Weiss, & D. F. Gray (San Francisco, CA: ASP), A20
Cesco, C. U., & Struve, O. 1946, ApJ, 104, 282
Chaplin, W. J., & Miglio, A. 2013, ARA&A, 51, 353
Chelli, A., Duvert, G., Bourgès, L., et al. 2016, A&A, 589, A112
Chojnowski, S. D., Hubrig, S., Hasselquist, S., et al. 2020, MNRAS, 496, 832
Claret, A. 2000, A&A, 363, 1081
Claret, A., & Torres, G. 2018, ApJ, 859, 100
Davis, J., Tango, W. J., & Booth, A. J. 2000, MNRAS, 318, 387
Demarque, P., Woo, J.-H., Kim, Y.-C., & Yi, S. K. 2004, ApJS, 155, 667
Eaton, J. A., & Williamson, M. H. 2004, Proc. SPIE, 5496, 710
Eaton, J. A., & Williamson, M. H. 2007, PASP, 119, 886
Fekel, F. C., Rajabi, S., Muterspaugh, M. W., et al. 2013, AJ, 145, 111
Fekel, F. C., Tomkin, J., & Williamson, M. H. 2009, AJ, 137, 3900
Gagné, J., Mamajek, E. E., Malo, L., et al. 2018, ApJ, 856, 23
Gaia Collaboration, Prusti, T., de Bruijne, J. H. J., et al. 2016, A&A, 595, A1
Gaia Collaboration, Vallenari, A., Brown, A. G. A., et al. 2022, arXiv:2208.00211
Gallenne, A., Kervella, P., Evans, N. R., et al. 2018, ApJ, 867, 121
Halbwachs, J.-L., Boffin, H. M. J., Le Bouquin, J.-B., et al. 2016, MNRAS, 455, 3303
Harper, W. E. 1926, PDAO, 3, 265
Hummel, C. A., Armstrong, J. T., Buscher, D. F., et al. 1995, AJ, 110, 376
Iglesias-Marzoa, R., López-Morales, M., & Jesús Arévalo Morales, M. 2015, PASP, 127, 567
Kochukhov, O., Khalack, V., Kobzar, O., et al. 2021, MNRAS, 506, 5328
Kołaczek-Szymański, P. A., Pigulski, A., Michalska, G., et al. 2021, A&A, 647, A12
Kolbas, V., Pavlovski, K., Southworth, J., et al. 2015, MNRAS, 451, 4150
Kluska, J., Kraus, S., Davies, C. L., et al. 2018, ApJ, 855, 44
Lester, K. V., Fekel, F. C., Muterspaugh, M., et al. 2020, AJ, 160, 58
Lester, K. V., Gies, D. R., Schaefer, G. H., et al. 2019a, AJ, 157, 140
Lester, K. V., Gies, D. R., Schaefer, G. H., et al. 2019b, AJ, 158, 218
Mayor, M., & Mazeh, T. 1987, A&A, 171, 157
Monnier, J. D., Zhao, M., Pedretti, E., et al. 2011, ApJL, 742, L1
Morales, L. M., Sandquist, E. L., Schaefer, G. H., et al. 2022, AJ, 164, 34
Nariai, K. 1970, PASJ, 22, 113
Paredes, L. A., Henry, T. J., Quinn, S. N., et al. 2021, AJ, 162, 176
Paxton, B., Bildsten, L., Dotter, A., et al. 2011, ApJS, 192, 3
Paxton, B., Smolec, R., Schwab, J., et al. 2019, ApJS, 243, 10
Petrie, R. M. 1937, PDAO, 6, 365
Pourbaix, D. 2000, A&AS, 145, 215
Prša, A., Harmanec, P., Torres, G., et al. 2016, AJ, 152, 41
Raghavan, D., McAlister, H. A., Henry, T. J., et al. 2010, ApJS, 190, 1
Richardson, N. D., Lee, L., Schaefer, G., et al. 2021, ApJL, 908, L3
Sandberg Lacy, C. H., & Fekel, F. C. 2011, AJ, 142, 185
Scarfe, C. D. 2010, Obs, 130, 214
Schaefer, G. H., Hummel, C. A., Gies, D. R., et al. 2016, AJ, 152, 213
Schlesinger, F. 1912, PAllO, 15, 139
Serenelli, A., Weiss, A., Aerts, C., et al. 2021, A&ARv, 29, 4
Skrutskie, M. F., Cutri, R. M., Stiening, R., et al. 2006, AJ, 131, 1163
Stassun, K. G., & Torres, G. 2018, ApJ, 862, 61
ten Brummelaar, T. A., McAlister, H. A., Ridgway, S. T., et al. 2005, ApJ, 628, 453
ten Brummelaar, T. A., Sturmann, J., Ridgway, S. T., et al. 2013, JAI, 2, 1340004
Thompson, G. I., Nandy, K., Jamar, C., et al. 1978, Catalogue of Stellar Ultraviolet Fluxes: a Compilation of Absolute Stellar Fluxes Measured by the Sky Survey Telescope (S2/68) Aboard the ESRO Satellite TD-1 (London: The Science Research Council)
Thompson, S. E., Everett, M., Mullally, F., et al. 2012, ApJ, 753, 86
Tokovinin, A., Fischer, D. A., Bonati, M., et al. 2013, PASP, 125, 1336
Tomkin, J., & Fekel, F. C. 2008, AJ, 135, 555
Torres, G., Andersen, J., & Giménez, A. 2010, A&ARv, 18, 67
Wang, S.-I., Hildebrand, R. H., Hobbs, L. M., et al. 2003, Proc. SPIE, 4841, 1145
Wright, E. L., Eisenhardt, P. R. M., Mainzer, A. K., et al. 2010, AJ, 140, 1868
Zacharias, N., Finch, C. T., Girard, T. M., et al. 2013, AJ, 145, 44
Zucker, S., & Mazeh, T. 1994, ApJ, 420, 806
Zucker, S., Mazeh, T., Santos, N. C., Udry, S., & Mayor, M. 2003, A&A, 404, 775